Article

Current Biology

Mitochondrial function regulates cell growth kinetics to maintain mitochondrial homeostasis

Graphical abstract

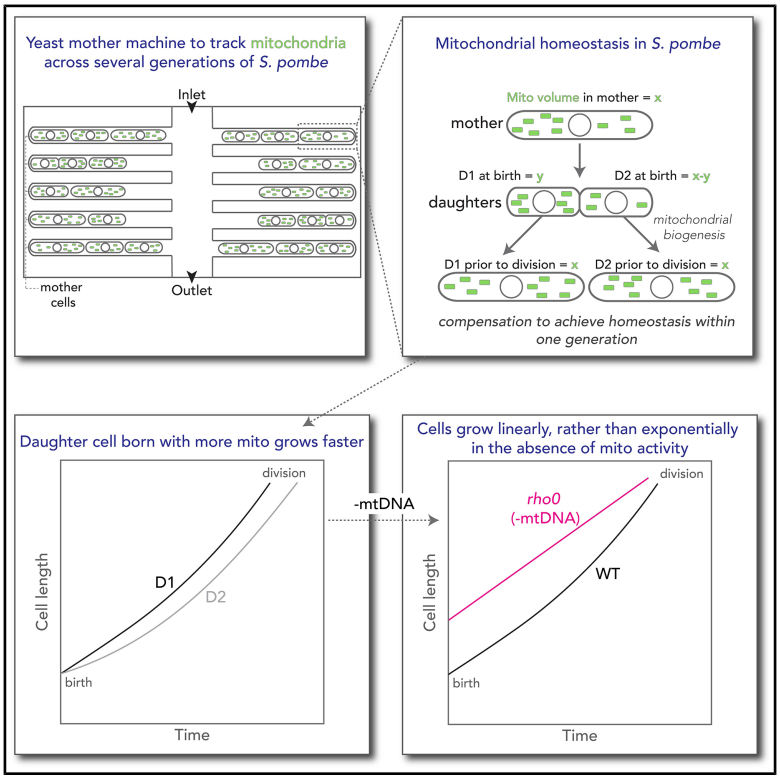

Highlights

- Mitochondrial volume added per cell cycle varies with mitochondrial volume at birth
- Mitochondrial volume at birth controls cell growth rate and thus timing of cell division
- Together, these ensure that mitochondrial homeostasis is maintained across generations
- Lack of mitochondrial activity drives linear rather than exponential cell growth

Authors

Leeba A. Chacko, Hidenori Nakaoka, Richard G. Morris, Wallace F. Marshall, Vaishnavi Ananthanarayanan

Correspondence

vaish@unsw.edu.au

In brief

Chacko et al. use a "mother machine" to track mitochondrial dynamics across generations of fission yeast, and they show that mitochondrial addition during the cell cycle is tuned to the mitochondrial volume at birth. This inherited mitochondrial volume dictates cell growth kinetics and ensures that mitochondrial homeostasis is achieved within one generation.

Chacko et al., 2025, Current Biology *35*, 5278–5288
November 3, 2025
https://doi.org/10.1016/j.cub.2025.09.046

CellPress

CellPress

Current Biology

Article

Mitochondrial function regulates cell growth kinetics to maintain mitochondrial homeostasis

Leeba A. Chacko,[1] Hidenori Nakaoka,[2] Richard G. Morris,[1,3,4] Wallace F. Marshall,[5] and Vaishnavi Ananthanarayanan[1,6,*]
[1]EMBL Australia Node in Single Molecule Science, Department of Molecular Medicine, School of Biomedical Sciences, University of New South Wales, Sydney, NSW 2052, Australia
[2]Department of Optical Imaging, Advanced Research Promotion Center, Tokushima University, 3-18-15 Kuramoto-cho, Tokushima City, 770-8503 Tokushima, Japan
[3]School of Physics, University of New South Wales, Sydney, NSW 2052, Australia
[4]ARC Centre of Excellence for the Mathematical Analysis of Cellular Systems, UNSW Node, Sydney, NSW 2052, Australia
[5]Department of Biochemistry and Biophysics, University of California, San Francisco, San Francisco, CA 94158, USA
[6]Lead contact
*Correspondence: vaish@unsw.edu.au
https://doi.org/10.1016/j.cub.2025.09.046

SUMMARY

Mitochondria are not produced *de novo* in newly divided daughter cells but are inherited from the mother cell during mitosis. While mitochondrial homeostasis is crucial for living cells, the feedback responses that maintain mitochondrial volume across generations of dividing cells remain elusive. Here, using a microfluidic yeast "mother machine," we tracked several generations of fission yeast cells and observed that cell size and mitochondrial volume grew exponentially during the cell cycle. We discovered that while mitochondrial homeostasis relied on the "sizer" mechanism of cell size maintenance, mitochondrial function was a critical determinant of the timing of cell division; cells born with lower-than-average amounts of mitochondria grew slower and thus added more mitochondria before they divided. Thus, mitochondrial addition during the cell cycle was tailored to the volume of mitochondria at birth, such that all cells ultimately contained the same mitochondrial volume at cell division. Quantitative modeling and experiments with mitochondrial DNA-deficient *rho0* cells additionally revealed that mitochondrial function was essential for driving the exponential growth of cells. Altogether, we demonstrate a central role for mitochondrial activity in dictating cellular growth rates and ensuring mitochondrial volume homeostasis.

INTRODUCTION

As a cell grows, the size or volume of organelles, such as the nucleus, lysosomes, and mitochondria, typically scales with cell size.[1–4] These scaling relationships are attributed to the differing functional demands on the organelle as the cell grows. However, the mechanisms that underpin organelle scaling and homeostasis are poorly understood. For example, while the importance of mitochondrial activity for cellular fitness is widely accepted,[5–8] it remains unclear how mitochondrial volume is maintained across successive generations.

Mitochondria typically form tubular networks that undergo continuous cycles of fusion and fission, enabling the redistribution of mitochondrial DNA (mtDNA) and the dilution or removal of damaged components.[9–11] Since mitochondria are composed of proteins that are encoded by both nuclear and mtDNA, mitochondria cannot be synthesized *de novo* in newly divided daughter cells but are partitioned into daughter cells from the mother. In fission yeast, we recently described an independent segregation mechanism for mitochondrial partitioning.[12] Mitochondria in mother cells undergo enhanced fission upon loss of microtubule association during closed mitosis in fission yeast, which increases mitochondrial copy numbers and thus reduces partitioning errors in this system.[12] Regardless, owing to the nature of the process, mitochondrial partitioning exhibited binomial errors,[13] resulting in slight differences in mitochondrial volumes at birth even in these symmetrically dividing cells.

Cell size homeostasis in fission yeast is achieved through the "sizer" mechanism, wherein cells sense their own size, and a critical size threshold is reached before cells undergo division.[14–16] Using mutants with varying widths, compared with wild-type (WT) cells, fission yeast has been found to undergo division upon reaching a defined surface area, in a process dependent on the protein kinase Cdr2.[16–18] Other systems, including bacteria and mammalian cells, behave as "adders," adding a constant length or mass during each cycle.[19,20] The key characteristics that determine the type of growth control are related to the duration of the G1 phase and the growth rate of cells in these periods.[21] Cells with a long G1 phase typically show sizer control, as seen in mouse epidermal stem cells.[22]

Recently, we discovered that fission yeast cells with mutations or deletions of proteins responsible for microtubule and mitochondrial dynamics exhibited a significant degree of asymmetric cell division.[23] Asymmetrically dividing cells still followed independent segregation, with the smaller daughter cell receiving less mitochondria from the mother than the larger daughter cell.

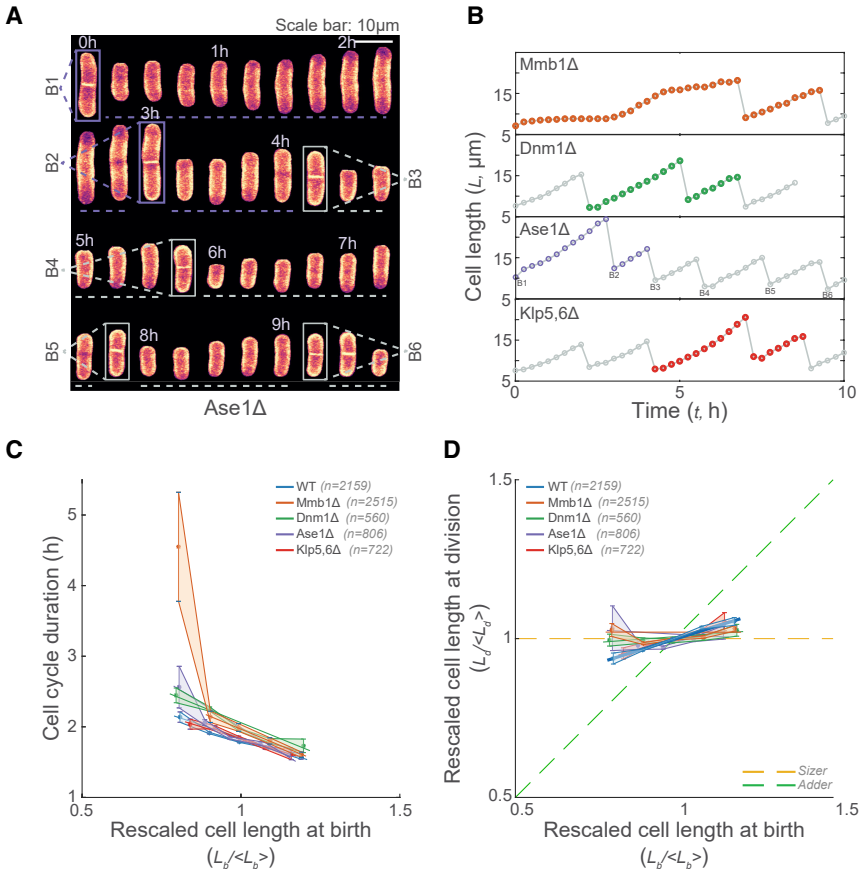

Figure 1. Mutants with a high degree of asymmetric division also exhibit "sizer-like" behavior

(A) Representative montage of an Ase1Δ cell (expressing a fluorescent membrane marker) undergoing growth and division in a single channel of the YMM.

(B) Plots of cell length (L) over time (t) for all the mutants indicated. Colored circles represent a long cell cycle followed by a short cycle. B1–B6 in the Ase1Δ plot represent six individual cell birth events as indicated in (A).

(C) Cell-cycle duration is inversely proportional to the cell size at birth, as shown by the cell-cycle duration plotted against the rescaled cell length at birth ($L_b/<L_b>$) in WT and mutant cells. Note that the Mmb1Δ fit was computed using only the last four bins, as the first bin contained several outliers.

(D) Rescaled cell length at division ($L_d/<L_d>$) plotted against rescaled cell length at birth in WT and mutant cells demonstrates that the sizer behavior is active in these cells. The yellow dashed line represents the expected data for a perfect sizer and the green dashed line that for an adder. The plots in (C) and (D) show mean ± SEM (solid circles and the shaded region, respectively) and their fits (solid lines). The data in (C) and (D) were rescaled to the mean of the parameters plotted as indicated in the axis labels. The slopes and R^2 values of the fits in (C) and (D) are in Table S2. Strains VA130, VA131, VA136, VA135, and VA144 were used for all figures in this panel (Table S3).

See also Figures S1 and S2, Table S1, and Video S2.

Occasionally, we observed mutant cells that partitioned their cytoplasm symmetrically but their mitochondria asymmetrically; in these cases, the daughter cell with less mitochondria grew slower than the other daughter. Given this key role of mitochondrial function in dictating cell growth and fitness, we asked how mitochondrial homeostasis is maintained across several generations of dividing cells.

Here, we use extended live-cell imaging in a yeast mother machine (YMM),[24,25] automated analysis, and quantitative modeling to demonstrate the critical role of mitochondrial function in determining not only feedback-driven mitochondrial homeostasis but also the timing of cell division, which ultimately controls cell size homeostasis in fission yeast.

RESULTS

Fission yeast cells achieve cell size homeostasis through the sizer mechanism

To visualize growth and division in several generations of fission yeast cells, we employed a YMM (Figure S1A). We confirmed that cells were healthy in the YMM, since the cell dimensions over the course of their cell cycle (Figure S1B; Video S1) were consistent with published literature.[26–30] Similarly, the cell lengths at birth (8.1 ± 0.8 μm; mean ± standard deviation [SD], n = 2,159 cells; Table S1) and at division (15.8 ± 1.4 μm; mean ± SD, n = 2,159 cells) were comparable to the known estimates in fission yeast cells,[26–29] and so was the mean duration of a cell cycle at 1.8 ± 0.3 h (mean ± SD, n = 2,159 cells; Figures S1C and S1D).

We then probed the size homeostasis mechanism in WT cells growing in the YMM and reconfirmed several previous findings suggesting that fission yeast cells show sizer-like behavior,[14,16,26,31] with cells that were smaller than the average length of ~8.1 μm at birth adding more length before division and vice versa (Figures S2A–S2C), ultimately resulting in cells initiating division at a characteristic size of 15.8 ± 1.4 μm (mean ± SD, n = 2,159; Figure S2D). Another consequence of the sizer-like behavior of fission yeast was that cells that were born smaller than average exhibited longer cell-cycle durations (Figure S2E), as reported previously.[32,33] We additionally confirmed that cellular volume, surface area, and length reported similarly on the cell size for the duration of the cell cycle (Figure S3A).

We previously showed that fission yeast cells with mutations or deletions of mitochondrial morphology-related proteins exhibit a higher degree of asymmetric cell division, compared with WT cells.[23] Cells devoid of microtubule-associated proteins are also known to exhibit asymmetric cell division.[12,34] We asked if these mutants that exhibit a high degree of asymmetric cell division also showed sizer-like behavior for cell size homeostasis. We observed that similar to WT cells, these mutant cells tailored their cell size at division to their size at birth—cells that were longer than average at birth divided faster in the following cycle to compensate for increased size at birth (Figures 1A–1C;

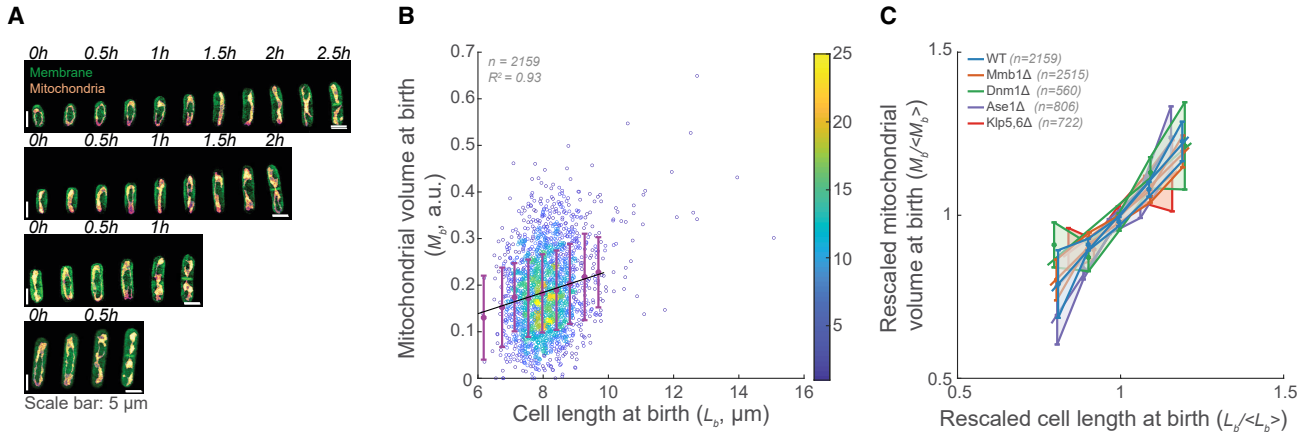

Figure 2. Mitochondrial volume at birth scales with cell length at birth

(A) Example montages of cell cycles of different-sized WT cells expressing fluorescent membrane and mitochondria markers.

(B) Mitochondrial volume at birth (M_b) plotted against cell length at birth (L_b) in WT cells reveals a linear scaling between the two parameters. Error bars represent SD, and the black solid line represents a linear fit to the data; the heatmap represents the density of the data.

(C) Rescaled mitochondrial volume at birth ($M_b / < M_b >$) plotted against rescaled cell length at birth ($L_b / < L_b >$) in mutant cells also demonstrates a similar linear relationship between cell size and mitochondrial volume at birth. The plots show mean ± SEM (solid circles and the shaded region, respectively) and their fits (solid lines). The data were rescaled as detailed in axis labels. The slopes and R^2 values of the fits are in Table S2. Strains VA130, VA131, VA136, VA135, and VA144 were used for this panel (Table S3).

See also Figure S3 and Videos S2 and S3.

Video S2). These asymmetrically dividing mutants also showed a characteristic division length, confirming their sizer-like behavior for size homeostasis (Figure 1D; Table S1).

Mitochondrial volume is proportional to cell size

We then probed mitochondrial volume in WT and mutant cells for the duration of their cell cycle (Video S3). We previously demonstrated that mitochondrial partitioning at division proceeds relative to daughter cell sizes.[23] Here, we tracked the mitochondrial volume alongside the cell sizes (Figure S3A) and observed that mitochondrial volume at birth scaled with the cell size at birth, such that a smaller cell than average contained less mitochondria at birth than a larger cell (Figures 2A and 2B). Mutant cells with higher degrees of asymmetric cell division also exhibited similar behavior (Figure S3B), with the mitochondrial volume inherited during division showing a linear relationship to cell length at birth (Figure 2C). It is striking that these mutants exhibited a scaling similar to that of WT, reinforcing the independent segregation mechanism underlying the partitioning of mitochondria in *S. pombe*.[12]

Mitochondrial volume at division exhibits compensatory signatures

Next, we asked how mitochondrial homeostasis was maintained across several generations. A previous study in fission yeast suggested that a constant volume of mitochondria is added during each cycle, irrespective of the mitochondrial volume at birth.[35] Alongside our data suggesting that mitochondrial volume at birth is dependent on cell size at birth (Figure 2), this would imply that even a cell that received less volume at birth (due to its smaller size) would add the same volume of mitochondria as a large cell. We measured the mitochondrial volume added during a cycle (by comparing the mitochondrial volume at division and at birth) and plotted this against the cell length at birth (Figure 3A). We observed that contrary to the proposed mechanism of constant volume addition, cells that were smaller than average at birth added more mitochondrial volume during their cell cycle. This resulted in cells, small and large, achieving similar mitochondrial volumes at division (Figure 3B), suggesting that rather than adding constant volume, cells exhibited compensation of mitochondrial volumes by adding more mitochondrial volume when born with less and vice versa. So too, the volume added per unit length before cell division was similar for cells with a wide range of starting mitochondrial concentrations (mitochondrial volume per unit length at birth) (Figure 3C), i.e., cells that were small at birth added more length (Figure S2C) *and* mitochondrial volume such that the ratio between the added mitochondrial volume and added cell length remained constant. We previously showed that cells that were smaller than average at birth had longer cell-cycle durations (Figure S2E). Accordingly, cells that had longer cell-cycle durations also added more mitochondria than those that had shorter cell-cycle durations (Figure S4A). The concentration of mitochondria at birth and division and added per unit length during the cycle remained fairly constant across a range of cell lengths at birth (Figures S4B–S4D), which fit with the compensatory homeostatic responses we observed.

Further, we split the WT cells into two populations, large and small cells, with the former having cell lengths >9 μm and the latter having cell lengths <7 μm at birth, i.e., 1 SD away from the mean length at birth. We tracked their cell lengths and mitochondrial volumes over the course of the cell cycle and observed that while the small cells started with lower cell lengths and mitochondrial volumes, they attained similar lengths and mitochondrial volumes as the large cells at the end of their cycle by prolonging their cell cycle (Figure 3D). Thus, fission yeast cells rely on the cell sizer mechanism to maintain mitochondrial homeostasis; larger (smaller) cells typically contain more (less)

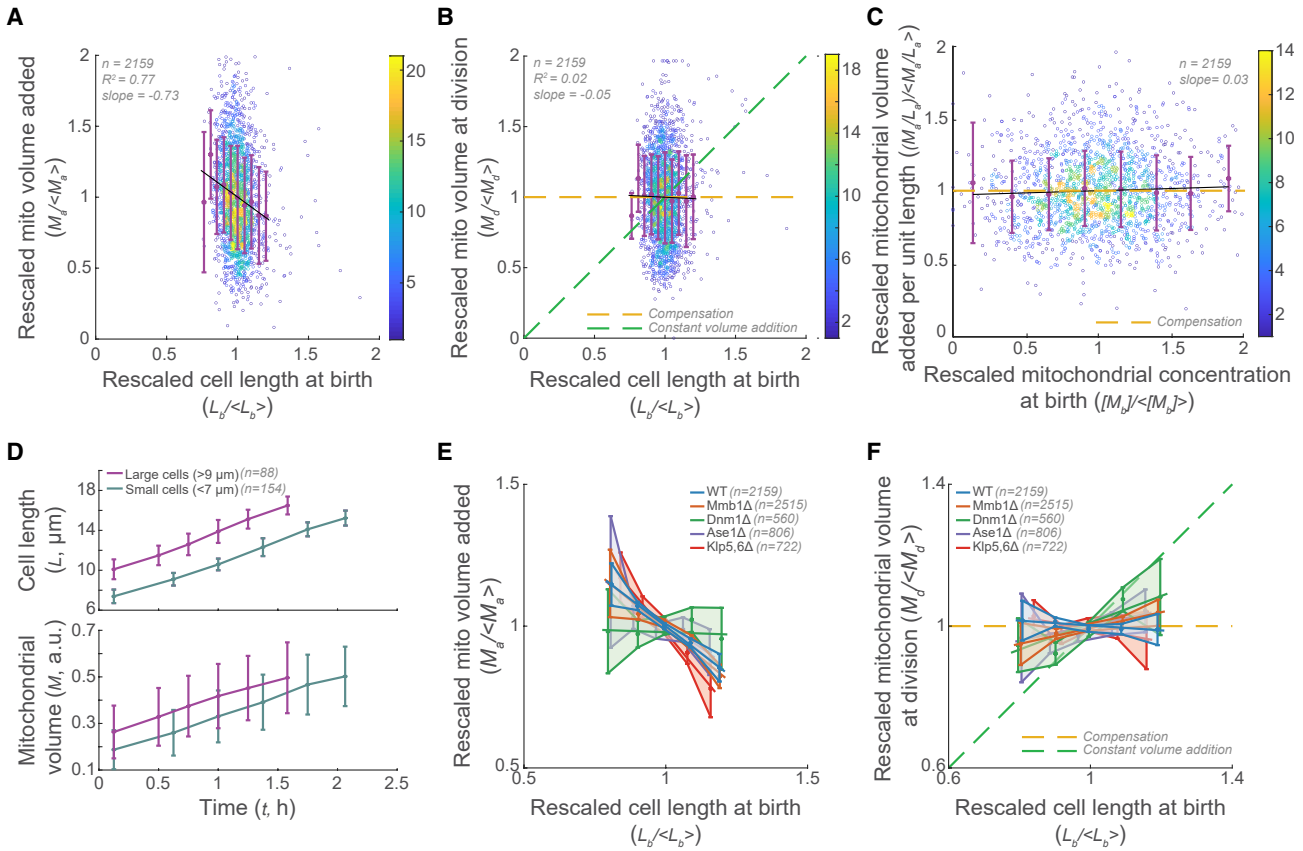

Figure 3. WT and mutant cells exhibit "compensation" of mitochondrial volume to achieve homeostasis

(A) Rescaled mitochondrial volume added in a cycle ($M_a/<M_a>$) plotted against the rescaled cell length at birth ($L_b/<L_b>$) in WT cells reveals an inverse relationship.

(B) Rescaled mitochondrial volume at division ($M_d/<M_d>$) plotted against the rescaled cell length at birth in WT cells demonstrates signatures of compensation, wherein all cells attain a typical mitochondrial volume at division.

(C) Rescaled mitochondrial volume added per unit length $((M_a/L_a)/<M_a/L_a>)$ added during the cell cycle plotted against the rescaled mitochondrial concentration at birth ($[M_b]/<[M_b]>$) in WT cells reveals a compensatory mechanism, with a constant volume of mitochondria added per unit length of cell.

In (A)–(C), error bars represent SD. Black solid lines represent linear fits to the data; the heatmap represents the density of the data.

(D) Cell length (top) and the mitochondrial volume (bottom) plotted over time in large (>9 μm, magenta) and small (<7 μm, teal) WT cells reveal differences in the duration of the cell cycle between the two populations. Error bars represent SD.

(E) Rescaled mitochondrial volumes added per cell cycle plotted against rescaled cell lengths at birth in mutant cells also show an inverse relationship.

(F) Rescaled mitochondrial volumes at division plotted against rescaled cell lengths at birth in mutant cells also demonstrate mitochondrial compensation.

In (B), (C), and (F), the yellow dashed line represents the expected data for a compensation mechanism and the green dashed line that for constant volume addition. The plots in (E) and (F) show mean ± SEM (solid circles and the shaded region, respectively) and their fits (solid lines). The data in (A)–(F) were rescaled as detailed in axis labels. The slopes and R^2 values of the fits in (E) and (F) are in Table S2. Strain VA130 was used for (A)–(D), and strains VA130, VA131, VA136, VA135, and VA144 were used in (E) and (F) (Table S3).

See also Figure S4.

mitochondria at birth but need to add less (more) cell size (length/area) before division, thus reducing (increasing) the amount of mitochondria added during the cell cycle. We observed similar behavior in mutant cells that have a higher propensity to divide asymmetrically, which showed an inverse relationship between cell length at birth and mitochondrial volume added during the cell cycle (Figure 3E), resulting in a characteristic mitochondrial volume at division across the population (Figure 3F). Thus, both WT and mutant cells corrected for deficiencies or excess mitochondrial volume in one generation, as indicated by the similar distributions of mitochondrial volumes at birth for these cells (Figures S4E–S4I).

Mitochondrial activity drives the exponential growth of cells and determines the timing of cell division

Thus far, we determined that mitochondrial homeostasis relies on the cell sizer mechanism. However, given the dependence of starting mitochondrial volume on cell size at birth, it remained unclear what the precise role of the sizer was in determining mitochondrial homeostasis. To delineate the specific role of mitochondrial activity, we chose to analyze daughter cell pairs in the WT population that divided symmetrically, i.e., had similar cytoplasmic volumes but exhibited asymmetric mitochondrial partitioning (Figure 4A). Such daughter cell pairs arose due to the nature of mitochondrial partitioning in fission yeast that

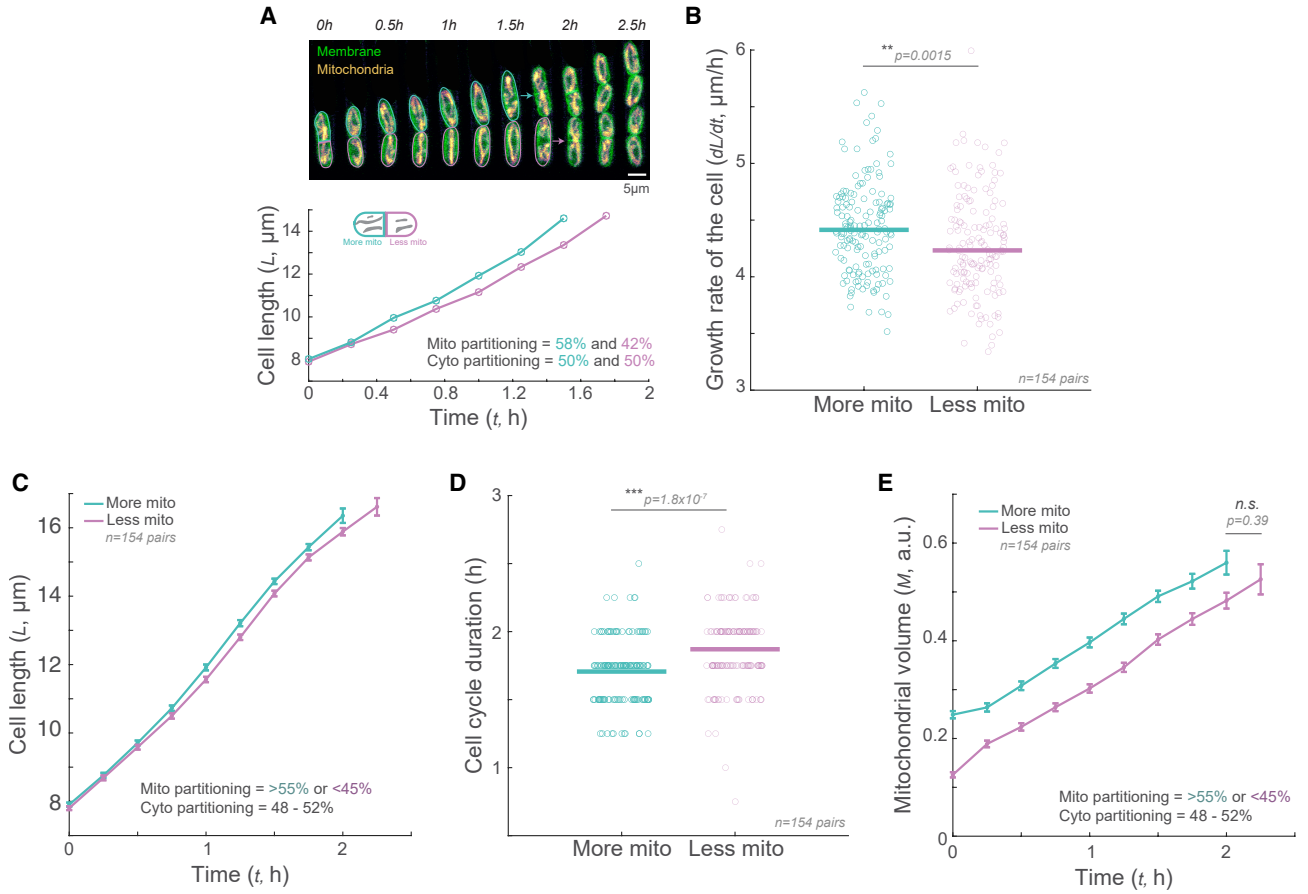

Figure 4. Mitochondrial activity determines the timing of cell division

(A) Top: montage of a representative pair of daughter cells that were born from symmetric division but asymmetric mitochondrial partitioning. Teal outlines the daughter cell with more mitochondria at birth and magenta, the daughter cell with less mitochondria. The teal arrow points to the division of the daughter cell born with more mitochondria, and magenta arrow points to the division of the daughter cell born with less mitochondria, showing the delay in the division of the latter. Bottom: cell length plotted over time for a representative pair of daughter cells born with similar cell sizes, but unequal mitochondrial volumes ("more mito" and "less mito," with 58% of the mother cell mitochondrial volume partitioned in the former and 42% partitioned in the latter but with both daughters having 50% of the mother cell length at division).

(B) Scatterplot of the growth rate of the cells that divided symmetrically but exhibited asymmetric mitochondrial partitioning. The horizontal lines represent the mean. The asterisks represent significance (**p = 0.0015; Mann-Whitney U test for non-parametric data).

(C) Cell length plotted over time for those pairs of cells whose cycles were tracked from birth to division, indicating a longer cell-cycle duration for those cells that had less mitochondrial volume at birth. The solid line represents the mean, and the error bars represent the SEM.

(D) Scatterplot of the cell-cycle duration of cells that divided symmetrically but exhibited asymmetric mitochondrial partitioning. The horizontal lines represent the mean. The asterisks represent significance (***$p = 1.8 \times 10^{-7}$; Mann-Whitney U test for non-parametric data).

(E) Mitochondrial volume plotted over time for those pairs of cells whose cycles were tracked fully, indicating both daughter cell pairs achieved similar mitochondrial volumes before division (n.s., not significant, p = 0.39; Mann-Whitney U test for non-parametric data). The solid line represents the mean, and the error bars represent the SEM. Strain VA130 was used for all panels in this figure (Table S3).

follows an independent segregation mechanism, with binomial errors.[12] Analysis of the cell lengths over time of these daughter cell pairs revealed that the cell with more mitochondria at birth grew significantly faster than the other daughter cell (Figure 4B), thus reaching the characteristic cell length for the sizer mechanism to operate sooner than the other daughter cell (Figure 4C). We calculated that the average cell-cycle duration of cells with "more mito" was 1.7 ± 0.2 h, while that of cells with "less mito" was 1.9 ± 0.2 h (mean ± SD; Figure 4D). This represents an average ~12% increase in cell-cycle durations in daughter cells that received less mitochondria at birth. We observed a similar inverse relationship between cell-cycle duration and mitochondrial concentration across the WT population (Figure S4J). Cells born with different starting mitochondrial volumes showed a similar mitochondrial volume at division (Figure 4E), indicating the presence of compensatory mechanisms.

To further explore the role of mitochondria in determining the growth kinetics and hence the timing of cell division, we tracked the change in cell length and mitochondrial volume over time in WT cells (Figure 5A). Measurement of the instantaneous growth rates of cells and the size-normalized instantaneous growth rates over time reconfirmed earlier findings that cells grow exponentially until mitosis in fission yeast (Figures 5B and S5A). Thereafter, the cellular growth rate slowed down considerably until cells

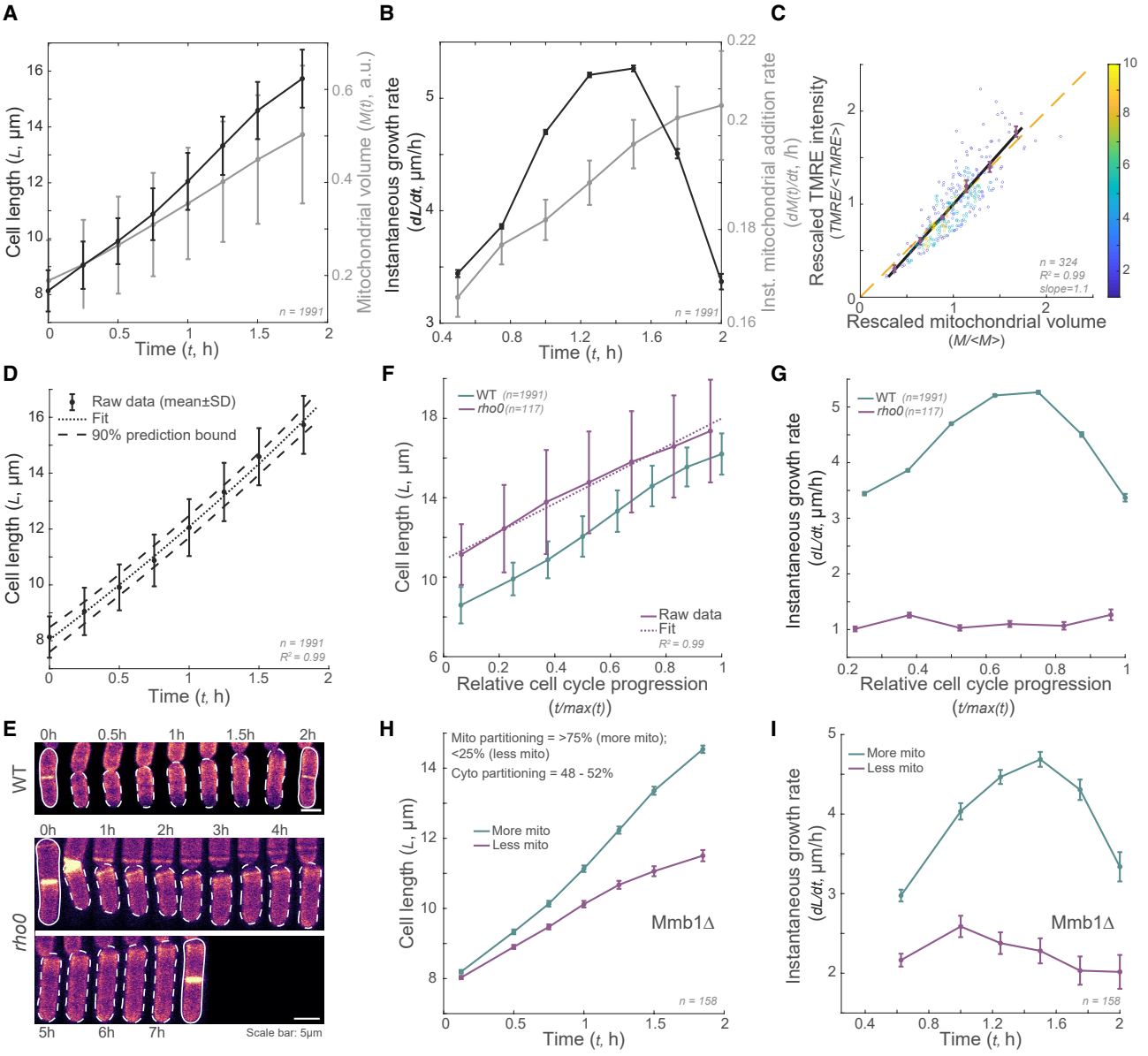

Figure 5. Loss of mitochondrial activity leads to linear cell growth

(A) Plots of cell length (L, black) and mitochondrial volume ($M(t)$, gray) over time for those cells whose durations are within one SD of the mean WT cell-cycle duration. Error bars represent SD.

(B) Plots of instantaneous growth rates of the cell ($dL(t)/dt$, black) and mitochondrial volume ($dM(t)/dt$, gray), respectively, for the cells analyzed in (A). Error bars represent SEM.

(C) Rescaled TMRE intensity ($TMRE/\langle TMRE\rangle$) of WT cells plotted against the rescaled mitochondrial volume ($M/\langle M\rangle$), showing a linear scaling between the two parameters. The black solid line represents a linear fit to the data; the heatmap represents the density of the data. Error bars represent SEM.

(D) Plot of cell length L over cell-cycle duration t. The dashed black line represents a fit to the equation $L(t) = 0.41k_2e^{0.51t} + Dt + E$. Error bars represent SD.

(E) Representative montages of a WT cell (top, expressing a fluorescent membrane marker) and *rho0* cell (bottom, stained with Calcofluor white) undergoing one cycle of growth and division.

(F) Plots of cell length over the relative cell-cycle duration ($t/max(t)$) for WT and *rho0* cells (teal and magenta, respectively) whose durations are within one SD of the mean WT and *rho0* cell-cycle durations, respectively. The dashed magenta line represents a fit to a polynomial with degree 1. Error bars represent SEM.

(G) Plots of instantaneous growth rates for WT and *rho0* cells (teal and magenta, respectively) for the cells analyzed in (D). Error bars represent SEM. In (F) and (G), data are plotted against the relative cell-cycle progression to aid comparison between cells with different cell-cycle durations.

(H) Plot of cell length over time for Mmb1Δ cells that divided symmetrically but partitioned mitochondria asymmetrically, showing a marked switch of cells that inherited <25% of the mother mitochondria to linear growth.

(I) Plot of instantaneous growth rate of cells over time for Mmb1Δ cells that divided symmetrically but partitioned mitochondria asymmetrically, demonstrating nearly constant growth rates in cells that inherited <25% of the mother mitochondria.

(legend continued on next page)

eventually divided. However, unlike cellular growth, mitochondrial addition rate continued to increase, implying an exponential increase in mitochondrial volume throughout the cell cycle (Figures 5B and S5B). Given our finding that in a daughter cell pair, the daughter that received more mitochondria from the mother grew faster (Figure 4B), we probed if the exponential growth of cells was driven by the exponential addition of mitochondria and the consequent exponential increase in mitochondrial activity. We first verified that mitochondrial activity was equivalent to mitochondrial volume in Tom20-GFP-expressing WT cells by quantifying the mitochondrial membrane potential, using the cationic dye tetramethylrhodamine ethyl ester (TMRE). Indeed, the TMRE intensity integrated over the whole cell scaled with the mitochondrial volume in WT cells (Figure 5C). Motivated by the increase in the mitochondrial addition rate across the cell cycle (Figures 5B and S5B), we modeled mitochondrial volume to increase exponentially over time. Specifically, we describe mitochondrial volume/activity M as

$$M(t) = m_0 e^{k_1 t}, \quad \text{(Equation 1)}$$

where m_0 is mitochondrial volume (or activity) at the start of the cell cycle, t is time, and k_1 is the mitochondrial volume addition rate.

The resulting fit to the raw data was highly robust, with an R^2 value of 0.99 (Figure S5C), confirming that an exponential model accurately captures the observed mitochondrial growth dynamics. From this fit, we extracted the values of m_0 and k_1.

Next, we modeled the growth rate of the cell (dL/dt) as dependent on the volume (or activity) of the mitochondria:

$$\frac{dL}{dt} = k_2 M(t) + D, \quad \text{(Equation 2)}$$

where k_2 is a rate constant that links mitochondrial activity to cell growth, and D is the mitochondrial activity-independent growth rate, likely dependent on glycolysis. Substituting Equation 1 and integrating Equation 2 gave

$$L(t) = \frac{k_2}{k_1} m_0 e^{k_1 t} + Dt + E, \quad \text{(Equation 3)}$$

where E is the integration constant. Given $m_0 = 0.21$ and $k_1 = 0.51$, we fit Equation 3 and obtained $k_2 = 3.60$, $D = 3.07$, and $E = 6.57$, with an R^2 value of 0.997, indicating an excellent correlation between the model and the experimental data (Figure 5D). This confirms that our model is sufficient to describe the dependence of the exponential growth of the cell on mitochondrial activity.

One implication of our model is that in the absence of mitochondrial activity, i.e., $M = 0$, rather than exhibiting exponential cell growth, cells would switch to linear growth, with a constant growth rate across the cell cycle. In other words, substituting $M = 0$ in Equation 2 such that

$$\frac{dL}{dt} = D, \text{ and } L(t) = Dt + E.$$

To test this, we employed fission yeast cells lacking mtDNA (*rho0*), which do not generate mitochondrial activity-derived ATP, and hence are known to grow much slower than WT cells.[36,37] Indeed, while mitochondria were visible in MitoTracker-stained *rho0* cells (Figure S5D), their activity was negligible compared with that of WT cells, as indicated by their weak TMRE staining (Figure S5E). We compared the cell lengths over time and growth rates of WT and *rho0* cells (Figure 5E) and measured a growth rate of only 1.1 ± 0.4 μm/h (mean ± SD, $n = 158$ cells) for the *rho0* cells as opposed to 3.8 ± 0.4 μm/h (mean ± SD, $n = 2{,}159$) in WT cells. Notably, while cell size increased exponentially until mitosis in WT cells, the growth rate was constant throughout the cell cycle in *rho0* cells, consistent with our quantitative model (Figures 5F and 5G). We confirmed that *rho0* cells switched to linear growth by plotting their size-normalized growth rate over time (Figures S5F and S5G).

We also observed that a small proportion of one of our mutants (lacking the microtubule-mitochondria linker protein, Mmb1) partitioned mitochondria between daugther cell pairs substantially asymmetrically while still dividing symmetrically (also characterized in our previous work[23]). We observed that the growth rate of the daughter cell that received very little mitochondria remained nearly constant throughout the cell cycle, while that of the other daughter cell increased during the first half (Figures 5H and 5I) similar to WT cells, reiterating the critical role of mitochondrial volume (or activity) in determining cellular growth kinetics.

DISCUSSION

In this work, we used a YMM to observe several generations of fission yeast cells undergoing growth and division (Figure S1). We first confirmed that both WT cells and mutant cells with a propensity for asymmetric cell division displayed sizer-like behavior, undergoing division at a characteristic size (Figures 1 and S2). While the sizer property of WT cells has been well established,[16–18,26,38] the fact that mutant cells demonstrate similar behavior is interesting, and it points to a decoupling of the machinery involved in establishing the cell division plane and that responsible for enforcing the sizer. We additionally observed that the cell-cycle duration is inversely proportional to cell size at birth (Figure 1C), as described previously.[26]

We quantified mitochondrial volume of cells from birth to division and discovered that while mitochondrial volume partitioning scaled with the birth size of the cell (cells that are small at birth typically have less mitochondria than large cells; Figures 2B and 2C), all cells attained similar mitochondrial volumes at division (Figures 3A, 3B, 3E, and 3F). This finding reveals a novel compensatory mechanism that corrects for initial mitochondrial "deficits" or "excesses." In an earlier study in *S. pombe*,[35] the authors concluded that mitochondrial volume homeostasis behaved like an adder wherein a constant volume of mitochondria was added per cycle, regardless of the starting mitochondrial volume. However, a deeper look at their data suggests that the authors may have in fact measured mitochondrial compensation similar to our data, since mitochondria volume (intensity) added

In (H) and (I), error bars represent SEM. The data in (C) were rescaled to the mean of the parameter plotted as indicated in the axis labels. Strain VA130 was used for (A), (B), and (D); strain VA134 was used for (C); strains VA130 and PHP14 were used for (E)–(G); and strain VA131 was used for (H) and (I) (Table S3).
See also Figure S5.

per unit length of growth during the cell cycle remained constant in their study (see Figure 4C in Jajoo et al.,[35] equivalent to Figure 3C in this manuscript). This would imply that a cell that added more length during the cycle (i.e., one that was short at birth) would also add more mitochondrial volume, which is in agreement with our data (Figures 3A and 3C). So too, if cells only added a constant volume of mitochondria per cycle, any deviation from the average mitochondrial volume at birth should take a few generations to converge back to the average volumes, as has been described for bacterial size regulation.[19] In contrast, we found that any deviation from mean mitochondrial volumes at birth was rectified within a single generation (Figures 3B, 3F, and S4E–S4I), which provides additional evidence of a compensatory mitochondrial homeostasis mechanism in these cells. Live-cell observations in *S. cerevisiae* have also revealed signatures of compensatory homeostasis, wherein a mother cell entering G1 with an abnormal mitochondrial volume relative to the total cell volume compensates by altering mitochondrial biogenesis to restore the correct ratio in the bud.[3]

Given the tight coupling in cells between cell size and mitochondrial volume, we sought to disentangle their specific roles in the process of mitochondrial homeostasis. We previously described mitochondrial volume as a critical determinant of cell growth rates[23] but did not follow the fates of cells with altered mitochondrial volumes at birth. Here, we discovered that in daughter cell pairs that partitioned their cytoplasm symmetrically but exhibited asymmetry in mitochondrial partitioning, the daughter cell with reduced mitochondrial volume showed slower growth rates (Figure 4). Other studies in mammalian cells report on similar phenomena, with daughter cells inheriting more mitochondria following cell division progressing faster through the cell cycle.[39] Here, we found that while cells with less (more) mitochondria grew slower (faster), all cells exhibited sizer-like behavior, dividing at similar sizes (Figure 4C). Thus, mitochondrial compensatory mechanisms determine the *time* at which the sizer is enforced, but the molecules and processes controlling the sizer likely operate independently of the mitochondrial volume at birth.

S. pombe growth rates have been described as linear, bilinear, exponential, and non-exponential.[15,27,30,40–43] With the high-throughput dataset we acquired, we found that the growth of cells fit best to exponential growth kinetics until cells entered mitosis (Figures 5B and S5A). We observed that mitochondrial volume also increased exponentially throughout the cell cycle (Figure S5B). This implies that mitochondrial volume feeds back to the biogenesis machinery with genes encoded by both nuclear and mtDNA to enable exponential growth.

We found a key difference between cellular growth rate and mitochondrial addition rate in cells, i.e., while cellular growth rates declined and eventually almost completely stalled during the later stages of a cell cycle, mitochondrial volume continued to add at an increasing rate for the entire cycle (Figures 5B, S5A, and S5B). Such increases in protein concentration while cells are stalled in mitosis have been described previously[44] and are essential for maintaining volume homeostasis. The slowing down of cell growth at the later stages is typically attributed to the cell having reached the characteristic size for the sizer mechanism to operate. However, lowered mitochondrial activity in cells as they approach mitosis might also contribute to their slower growth rates. Such lowering of mitochondrial activity (specifically ATP synthesis) during early stages of mitosis has been observed in other cells.[45] Using quantitative modeling, we demonstrated that exponential growth of cells early in the cell cycle depended on mitochondrial volume (or activity) in WT cells (Figure 5D). Our model also assumes that linear growth of cells is devoid of mitochondrial activity. Therefore, we tested our model in cells lacking mtDNA, and consistent with our assumption, we observed that *rho0* cells displayed growth that fit to linear kinetics, with a constant growth rate across the cell cycle (Figures 5F and 5G). Similarly, in Mmb1Δ daughter cell pairs, which partitioned the mother cell cytoplasm symmetrically but mitochondria highly asymmetrically, we observed a marked difference between the growth kinetics of cells that contained little mitochondria and that of the cells that were apportioned more mitochondria (Figures 5H and 5I). Although we implemented linear growth for cells without mitochondrial activity in our model, we note that other growth kinetics may also be compatible with the data. We also acknowledge that the model is largely post hoc, designed to capture experimentally observed links between mitochondrial activity and cell growth rates, rather than derived from a detailed theoretical framework. Additional investigations and theoretical analyses (for example, in cells with mitochondrial mutations leading to less severe growth defects than *rho0* cells) will be needed to test whether our conclusions translate more broadly.

Which aspects of mitochondrial function are relevant for the modulation of cell growth kinetics? An intuitive answer would be energy production, since *rho0* cells lack the ability to generate mitochondrial ATP[36] (Figure S5E). Other studies support this conclusion, since increased mitochondrial mass leads to increased rates of energy-dependent transcription and translation.[39,46] However, the reduced mitochondrial membrane potential in *rho0* cells could result in altered reactive oxygen species (ROS) levels, which have also been shown to affect cell proliferation.[47] So too, *rho0* 143B.TK-osteosarcoma cells become auxotrophic for uridine and pyruvate after a few days in culture due to sustained abrogation of oxidative phosphorylation, thus affecting nucleotide synthesis in addition to energy production in these cells.[48] In budding yeast, the slow growth of *rho0* cells has been attributed to the defective biosynthesis of key amino acids.[49] Future studies will help identify the precise molecules and machinery that participate in the crosstalk between mitochondrial function and cell growth. While it has been established in several systems that mitochondrial volume and mtDNA scale with cell size,[3,50,51] here, we additionally show that mitochondrial volume is a key determinant of *when* the size control mechanisms are invoked.

In summary, our findings reveal a robust mechanism of mitochondrial homeostasis governed by mitochondrial activity; when cells inherit a lower-than-average mitochondrial volume, they compensate by extending their cell cycle, thereby synthesizing additional mitochondria before dividing in accordance with the sizer mechanism. This compensatory strategy preserves mitochondrial homeostasis over multiple generations of dividing cells.

RESOURCE AVAILABILITY

Lead contact

Further information and requests for resources and reagents should be directed to and will be fulfilled by the lead contact, Dr. Vaishnavi Ananthanarayanan (vaish@unsw.edu.au).

Materials availability

All reagents generated in this study are available from the lead contact without restriction.

Data and code availability

- All data are provided in the manuscript.
- This paper does not report original code.
- Any additional information required to reanalyze the data reported in this paper is available from the lead contact upon request.

ACKNOWLEDGMENTS

We thank the Katharina Gaus Light Microscopy Facility, UNSW, Australia, for the use of the Nikon A1, AX-R confocal microscopes, and data analysis computer; P. Delivani (Max Planck Institute of Molecular Cell Biology and Genetics, Dresden, Germany), S. Martin (University of Geneva, Switzerland), Tomoyuki Fukuda (Niigata University Graduate School of Medical and Dental Sciences, Niigata, Japan), J. Friedman (UT Southwestern Medical Center, USA), M. Takaine (Gunma University, Gunma, Japan), I. Tolić (Ruđer Bošković Institute, Zagreb, Croatia), P. Tran (University of Pennsylvania, Philadelphia, PA, USA), T.D. Fox (Cornell University, Ithaca, NY, USA), and National BioResource Project Japan for yeast strains and constructs; EMBL Australia for funding to V.A. and R.G.M.; Australian Research Council Centre of Excellence for Mathematical Analysis of Cellular Systems (CE230100001) for funding to R.G.M.; and the NIH (grant R35 GM130327) for funding to W.F.M.

AUTHOR CONTRIBUTIONS

Conceptualization, V.A.; data curation, L.A.C. and V.A.; formal analysis, L.A.C., R.G.M., W.F.M., and V.A.; funding acquisition, V.A.; investigation, L.A.C.; methodology, L.A.C., H.N., and V.A.; project administration, V.A.; resources, H.N. and V.A.; software, L.A.C. and V.A.; supervision, V.A.; validation, L.A.C. and V.A.; visualization, L.A.C. and V.A.; writing – original draft, V.A.; writing – review & editing, L.A.C., H.N., R.G.M., W.F.M., and V.A.

DECLARATION OF INTERESTS

W.F.M. is a member of *Current Biology*'s advisory board.

STAR★METHODS

Detailed methods are provided in the online version of this paper and include the following:

- KEY RESOURCES TABLE
- EXPERIMENTAL MODEL AND SUBJECT DETAILS
- METHOD DETAILS
  - Construction of strains
  - Preparing the YMM mold
  - Preparing the YMM
  - Preparing *S. pombe* for imaging in the YMM
  - Live-cell imaging using the YMM
  - MitoTracker and TMRE staining
  - Measurement of surface area and volume of *S. pombe* cells
- QUANTIFICATION AND STATISTICAL ANALYSIS
  - Image Analysis
  - Statistical analysis

SUPPLEMENTAL INFORMATION

Supplemental information can be found online at https://doi.org/10.1016/j.cub.2025.09.046.

Received: March 20, 2025
Revised: August 8, 2025
Accepted: September 17, 2025
Published: October 15, 2025

REFERENCES

1. Neumann, F.R., and Nurse, P. (2007). Nuclear size control in fission yeast. J. Cell Biol. *179*, 593–600. https://doi.org/10.1083/jcb.200708054.
2. Jorgensen, P., Edgington, N.P., Schneider, B.L., Rupes, I., Tyers, M., and Futcher, B. (2007). The size of the nucleus increases as yeast cells grow. Mol. Biol. Cell *18*, 3523–3532. https://doi.org/10.1091/mbc.e06-10-0973.
3. Rafelski, S.M., Viana, M.P., Zhang, Y., Chan, Y.H.M., Thorn, K.S., Yam, P., Fung, J.C., Li, H., da Costa, F., and Marshall, W.F. (2012). Mitochondrial network size scaling in budding yeast. Science *338*, 822–824. https://doi.org/10.1126/science.1225720.
4. Uchida, M., Sun, Y., McDermott, G., Knoechel, C., Le Gros, M.A.L., Parkinson, D., Drubin, D.G., and Larabell, C.A. (2011). Quantitative analysis of yeast internal architecture using soft x-ray tomography. Yeast Chichester Engl. *28*, 227–236. https://doi.org/10.1002/yea.1834.
5. Embley, T.M., and Martin, W. (2006). Eukaryotic evolution, changes and challenges. Nature *440*, 623–630. https://doi.org/10.1038/nature04546.
6. Dua, N., Seshadri, A., and Badrinarayanan, A. (2022). Dart-mediated mtdna damage induces dynamic reorganization and selective segregation of mitochondria. J. Cell Biol. *221*, e202205104. https://doi.org/10.1083/jcb.202205104.
7. Fu, C., Jain, D., Costa, J., Velve-Casquillas, G., and Tran, P.T. (2011). mmb1p binds mitochondria to dynamic microtubules. Curr. Biol. *21*, 1431–1439. https://doi.org/10.1016/j.cub.2011.07.013.
8. Vercellino, I., and Sazanov, L.A. (2022). The assembly, regulation and function of the mitochondrial respiratory chain. Nat. Rev. Mol. Cell Biol. *23*, 141–161. https://doi.org/10.1038/s41580-021-00415-0.
9. Shah, M., Chacko, L.A., Joseph, J.P., and Ananthanarayanan, V. (2021). Mitochondrial dynamics, positioning and function mediated by cytoskeletal interactions. Cell. Mol. Life Sci. *78*, 3969–3986. https://doi.org/10.1007/s00018-021-03762-5.
10. Hu, C., Huang, Y., and Li, L. (2017). Drp1-dependent mitochondrial fission plays critical roles in physiological and pathological progresses in mammals. Int. J. Mol. Sci. *18*, 144. https://doi.org/10.3390/ijms18010144.
11. Ul Fatima, N.U., and Ananthanarayanan, V. (2023). Mitochondrial movers and shapers: Recent insights into regulators of fission, fusion and transport. Curr. Opin. Cell Biol. *80*, 102150. https://doi.org/10.1016/j.ceb.2022.102150.
12. Mehta, K., Chacko, L.A., Chug, M.K., Jhunjhunwala, S., and Ananthanarayanan, V. (2019). Association of mitochondria with microtubules inhibits mitochondrial fission by precluding assembly of the fission protein dnm1. J. Biol. Chem. *294*, 3385–3396. https://doi.org/10.1074/jbc.RA118.006799.
13. Birky, C.W. (2001). The inheritance of genes in mitochondria and chloroplasts: Laws, mechanisms, and models. Annu. Rev. Genet. *35*, 125–148. https://doi.org/10.1146/annurev.genet.35.102401.090231.
14. Wood, E., and Nurse, P. (2015). Sizing up to divide: Mitotic cell-size control in fission yeast. Annu. Rev. Cell Dev. Biol. *31*, 11–29. https://doi.org/10.1146/annurev-cellbio-100814-125601.
15. Jia, C., Singh, A., and Grima, R. (2022). Characterizing non-exponential growth and bimodal cell size distributions in fission yeast: An analytical approach. PLoS Comp. Biol. *18*, e1009793. https://doi.org/10.1371/journal.pcbi.1009793.
16. Facchetti, G., Knapp, B., Chang, F., and Howard, M. (2019). Reassessment of the basis of cell size control based on analysis of cell-to-cell variability. Biophys. J. *117*, 1728–1738. https://doi.org/10.1016/j.bpj.2019.09.031.
17. Pan, K.Z., Saunders, T.E., Flor-Parra, I., Howard, M., and Chang, F. (2014). Cortical regulation of cell size by a sizer cdr2p. eLife *3*, e02040. https://doi.org/10.7554/eLife.02040.
18. Miller, K.E., Vargas-Garcia, C., Singh, A., and Moseley, J.B. (2023). The fission yeast cell size control system integrates pathways measuring cell

surface area, volume, and time. Curr. Biol. *33*, 3312–3324.e7. https://doi.org/10.1016/j.cub.2023.06.054.

19. Taheri-Araghi, S., Bradde, S., Sauls, J.T., Hill, N.S., Levin, P.A., Paulsson, J., Vergassola, M., and Jun, S. (2015). Cell-size control and homeostasis in bacteria. Curr. Biol. *25*, 385–391. https://doi.org/10.1016/j.cub.2014.12.009.
20. Varsano, G., Wang, Y., and Wu, M. (2017). Probing mammalian cell size homeostasis by channel-assisted cell reshaping. Cell Rep. *20*, 397–410. https://doi.org/10.1016/j.celrep.2017.06.057.
21. Cadart, C., Monnier, S., Grilli, J., Sáez, P.J., Srivastava, N., Attia, R., Terriac, E., Baum, B., Cosentino-Lagomarsino, M., and Piel, M. (2018). Size control in mammalian cells involves modulation of both growth rate and cell cycle duration. Nat. Commun. *9*, 3275. https://doi.org/10.1038/s41467-018-05393-0.
22. Proulx-Giraldeau, F., Skotheim, J.M., and François, P. (2022). Evolution of cell size control is canalized towards adders or sizers by cell cycle structure and selective pressures. eLife *11*, e79919. https://doi.org/10.7554/eLife.79919.
23. Chacko, L.A., Mikus, F., Ariotti, N., Dey, G., and Ananthanarayanan, V. (2023). Microtubule–mitochondrial attachment facilitates cell division symmetry and mitochondrial partitioning in fission yeast. J. Cell Sci. *136*, jcs260705. https://doi.org/10.1242/jcs.260705.
24. Nakaoka, H., and Wakamoto, Y. (2017). Aging, mortality, and the fast growth trade-off of schizosaccharomyces pombe. PLoS Biol. *15*, e2001109. https://doi.org/10.1371/journal.pbio.2001109.
25. Nakaoka, H. (2025). Live imaging of fission yeast single-cell lineages using a microfluidic device. Methods Mol. Biol. *2862*, 61–76. https://doi.org/10.1007/978-1-0716-4168-2_5.
26. Fantes, P.A. (1977). Control of cell size and cycle time in *Schizosaccharomyces pombe*. J. Cell Sci. *24*, 51–67. https://doi.org/10.1242/jcs.24.1.51.
27. Mitchison, J.M., and Nurse, P. (1985). Growth in cell length in the fission yeast *Schizosaccharomyces* pombe. J. Cell Sci. *75*, 357–376. https://doi.org/10.1242/jcs.75.1.357.
28. Pérez, P., Cortés, J.C.G., Cansado, J., and Ribas, J.C. (2018). Fission yeast cell wall biosynthesis and cell integrity signalling. Cell Surf. *4*, 1–9. https://doi.org/10.1016/j.tcsw.2018.10.001.
29. Piel, M., and Tran, P.T. (2009). Cell shape and cell division in fission yeast. Curr. Biol. *19*, R823–R827. https://doi.org/10.1016/j.cub.2009.08.012.
30. Knapp, B.D., Odermatt, P., Rojas, E.R., Cheng, W., He, X., Huang, K.C., and Chang, F. (2019). Decoupling of rates of protein synthesis from cell expansion leads to supergrowth. Cell Syst. *9*, 434–445.e6. https://doi.org/10.1016/j.cels.2019.10.001.
31. Nurse, P. (1975). Genetic control of cell size at cell division in yeast. Nature *256*, 547–551. https://doi.org/10.1038/256547a0.
32. Nasmyth, K., Nurse, P., and Fraser, R.S.S. (1979). The effect of cell mass on the cell cycle timing and duration of *s*-phase in fission yeast. J. Cell Sci. *39*, 215–233. https://doi.org/10.1242/jcs.39.1.215.
33. Hayles, J., and Nurse, P. (2018). Introduction to fission yeast as a model system. Cold Spring Harbor Protoc. *2018*, 079749. https://doi.org/10.1101/pdb.top079749.
34. Jain, I., Rao, M., and Tran, P.T. (2023). Reliable and robust control of nucleus centering is contingent on nonequilibrium force patterns. iScience *26*, 106665. https://doi.org/10.1016/j.isci.2023.106665.
35. Jajoo, R., Jung, Y., Huh, D., Viana, M.P., Rafelski, S.M., Springer, M., and Paulsson, J. (2016). Accurate concentration control of mitochondria and nucleoids. Science *351*, 169–172. https://doi.org/10.1126/science.aaa8714.
36. Haffter, P., and Fox, T.D. (1992). Nuclear mutations in the petite-negative yeast schizosaccharomyces pombe allow growth of cells lacking mitochondrial dna. Genetics *131*, 255–260. https://doi.org/10.1093/genetics/131.2.255.
37. Chacko, L.A., Mehta, K., and Ananthanarayanan, V. (2019). Cortical tethering of mitochondria by the anchor protein mcp5 enables uniparental inheritance. J. Cell Biol. *218*, 3560–3571. https://doi.org/10.1083/jcb.201901108.
38. Sveiczer, A., Novak, B., and Mitchison, J.M. (1996). The size control of fission yeast revisited. J. Cell Sci. *109*, 2947–2957. https://doi.org/10.1242/jcs.109.12.2947.
39. das Neves, R.P., Jones, N.S., Andreu, L., Gupta, R., Enver, T., and Iborra, F.J. (2010). Connecting variability in global transcription rate to mitochondrial variability. PLoS Biol. *8*, e1000560. https://doi.org/10.1371/journal.pbio.1000560.
40. Cooper, S. (2006). Distinguishing between linear and exponential cell growth during the division cycle: Single-cell studies, cell-culture studies, and the object of cell-cycle research. Theor. Biol. Med. Model. *3*, 10. https://doi.org/10.1186/1742-4682-3-10.
41. Buchwald, P., and Sveiczer, A. (2006). The time-profile of cell growth in fission yeast: model selection criteria favoring bilinear models over exponential ones. Theor. Biol. Med. Model. *3*, 16. https://doi.org/10.1186/1742-4682-3-16.
42. Mitchison, J.M. (2003). Growth during the cell cycle. Int. Rev. Cytol. *226*, 165–258. https://doi.org/10.1016/S0074-7696(03)01004-0.
43. Baumgärtner, S., and Tolić-Nørrelykke, I.M. (2009). Growth pattern of single fission yeast cells is bilinear and depends on temperature and dna synthesis. Biophys. J. *96*, 4336–4347. https://doi.org/10.1016/j.bpj.2009.02.051.
44. Odermatt, P.D., Miettinen, T.P., Lemière, J., Kang, J.H., Bostan, E., Manalis, S.R., Huang, K.C., and Chang, F. (2021). Variations of intracellular density during the cell cycle arise from tip-growth regulation in fission yeast. eLife *10*, e64901. https://doi.org/10.7554/eLife.64901.
45. Kang, J.H., Katsikis, G., Li, Z., Sapp, K.M., Stockslager, M.A., Lim, D., Vander Heiden, M.G.V., Yaffe, M.B., Manalis, S.R., and Miettinen, T.P. (2020). Monitoring and modeling of lymphocytic leukemia cell bioenergetics reveals decreased atp synthesis during cell division. Nat. Commun. *11*, 4983. https://doi.org/10.1038/s41467-020-18769-y.
46. Guantes, R., Rastrojo, A., Neves, R., Lima, A., Aguado, B., and Iborra, F.J. (2015). Global variability in gene expression and alternative splicing is modulated by mitochondrial content. Genome Res. *25*, 633–644. https://doi.org/10.1101/gr.178426.114.
47. Martínez-Reyes, I., Diebold, L.P., Kong, H., Schieber, M., Huang, H., Hensley, C.T., Mehta, M.M., Wang, T., Santos, J.H., Woychik, R., et al. (2016). Tca cycle and mitochondrial membrane potential are necessary for diverse biological functions. Mol. Cell *61*, 199–209. https://doi.org/10.1016/j.molcel.2015.12.002.
48. King, M.P., and Attardi, G. (1989). Human cells lacking mtdna: Repopulation with exogenous mitochondria by complementation. Science *246*, 500–503. https://doi.org/10.1126/science.2814477.
49. Vowinckel, J., Hartl, J., Marx, H., Kerick, M., Runggatscher, K., Keller, M.A., Mülleder, M., Day, J., Weber, M., Rinnerthaler, M., et al. (2021). The metabolic growth limitations of petite cells lacking the mitochondrial genome. Nat. Metab. *3*, 1521–1535. https://doi.org/10.1038/s42255-021-00477-6.
50. Posakony, J.W., England, J.M., and Attardi, G. (1977). Mitochondrial growth and division during the cell cycle in hela cells. J. Cell Biol. *74*, 468–491. https://doi.org/10.1083/jcb.74.2.468.
51. Seel, A., Padovani, F., Mayer, M., Finster, A., Bureik, D., Thoma, F., Osman, C., Klecker, T., and Schmoller, K.M. (2023). Regulation with cell size ensures mitochondrial dna homeostasis during cell growth. Nat. Struct. Mol. Biol. *30*, 1549–1560. https://doi.org/10.1038/s41594-023-01091-8.
52. Schindelin, J., Arganda-Carreras, I., Frise, E., Kaynig, V., Longair, M., Pietzsch, T., Preibisch, S., Rueden, C., Saalfeld, S., Schmid, B., et al. (2012). Fiji: an open-source platform for biological-image analysis. Nat. Methods *9*, 676–682. https://doi.org/10.1038/nmeth.2019.
53. Arganda-Carreras, I., Kaynig, V., Rueden, C., Eliceiri, K.W., Schindelin, J., Cardona, A., and Sebastian Seung, H. (2017). Trainable weka segmentation: a machine learning tool for microscopy pixel classification. Bioinformatics *33*, 2424–2426. https://doi.org/10.1093/bioinformatics/btx180.

54. Stringer, C., Wang, T., Michaelos, M., and Pachitariu, M. (2021). Cellpose: a generalist algorithm for cellular segmentation. Nat. Methods *18*, 100–106. https://doi.org/10.1038/s41592-020-01018-x.

55. Forsburg, S.L., and Rhind, N. (2006). Basic methods for fission yeast. Yeast *23*, 173–183. https://doi.org/10.1002/yea.1347.

56. Fankhauser, C., and Simanis, V. (1993). The schizosaccharomyces pombe cdc14 gene is required for septum formation and can also inhibit nuclear division. Mol. Biol. Cell *4*, 531–539. https://doi.org/10.1091/mbc.4.5.531.

57. Jin, Q.W., and McCollum, D. (2003). Scw1p antagonizes the septation initiation network to regulate septum formation and cell separation in the fission yeast schizosaccharomyces pombe. Eukaryot. Cell *2*, 510–520. https://doi.org/10.1128/EC.2.3.510-520.2003.

58. Stolz, J., Caspari, T., Carr, A.M., and Sauer, N. (2004). Cell division defects of schizosaccharomyces pombe liz1- mutants are caused by defects in pantothenate uptake. Eukaryot. Cell *3*, 406–412. https://doi.org/10.1128/EC.3.2.406-412.2004.

59. Pérez, P., Cortés, J.C.G., Martín-García, R., and Ribas, J.C. (2016). Overview of fission yeast septation. Cell. Microbiol. *18*, 1201–1207. https://doi.org/10.1111/cmi.12611.

60. Carlson, C.R., Grallert, B., Stokke, T., and Boye, E. (1999). Regulation of the start of dna replication in schizosaccharomyces pombe. J. Cell Sci. *112*, 939–946. https://doi.org/10.1242/jcs.112.6.939.

61. Lukas (2025). Heatscatter plot for variables x and y. MATLAB Central File Exchange.

62. Campbell, R. (2025). raacampbell/shadederrorbar. GitHub. https://github.com/raacampbell/shadedErrorBar.

STAR★METHODS

KEY RESOURCES TABLE

REAGENT or RESOURCE	SOURCE	IDENTIFIER
Chemicals, peptides, and recombinant proteins		
MitoTracker Orange CMTMRos	Thermo Scientific	Cat. # M7510
Tetramethylrhodamine, Ethyl Ester, Perchlorate (TMRE)	Thermo Scientific	Cat. # T669
Calcofluor white	Sigma-Aldrich	Cat. #18909-100ML-F
Experimental models: Organisms/strains		
h- dnm1::kanr leu1 32ade-	Yannick Gachet, Toulouse	Dnm1Δ
h- leu1 ura4 his7 Δklp5::ura4+ Δklp6::ura4+	YGRC, Japan	FY20823
h- Δ klp5- Δklp6 – nmt1-GFP-atb2 leu ade	Rafael Carazo Salas, UK	G3B
h+ tom20-GFP:KanR	Jonathan Friedman, UT Southwestern, Dallas, Texas, USA	JFY2975
h- tom20-mCherry:NatR	Jonathan Friedman, UT Southwestern, Dallas, Texas, USA	JFY3062
h+ sid4-GFP::kan r kan r -nmtP3-GFP-atb2+ nmt1-pCOX4-RFP::leu1+ ura4-D18 ade6-M210	Iva Tolić	KI001
h- WT	Iva Tolić	L972
h- rho0 ade6M-216 leu1-32 ptp1-1	Thomas Fox, Cornell University, USA	PHP14
h+ mmb1 Δ:Kanr cox4-GFP:leu2 mCherry-atb2:Hygr ade6-m210 leu1-32 ura4-d18	Phong Tran, University of Pennsylvania, USA	PT2244
h- ase1::kanMX6 leu1-32 ura4-D18	Phong Tran, University of Pennsylvania, USA	PT592
h+ mmb1Δ:Kanr	This manuscript	VA078
h+ ura4+::pact1:sfGFP-3RitCb: terminatortdh1 leu-	This manuscript	VA128
h- ura4+::pact1:sfGFP-3RitCb: terminatortdh1 Tom20-mCherry:NatR	This manuscript	VA130
h+ mmb1Δ:Kanr ura4+::pact1:sfGFP-3RitCb:terminatortdh1 Tom20-mCherry: NatR	This manuscript	VA131
h- ase1::kanMX6 leu1-32 ura4-D18 Tom20-mCherry:NatR	This manuscript	VA132
h- tom20-GFP:KanR	This manuscript	VA134
h- ase1::kanMX6 Tom20-mCherry:NatR ura4+::pact1:sfGFP-3RitCb:terminatortdh1	This manuscript	VA135
h+ dnm1::kanr ura4+::pact1:sfGFP-3RitCb: terminatortdh1 Tom20-mCherry:NatR	This manuscript	VA136
h- Δklp5::ura4+ Δklp6::ura4+ Tom20-mCherry:NatR	This manuscript	VA144
h- ura4+::pact1:sfGFP-3RitCb: terminatortdh1 ade6-M210 leu+	Sophie Martin, University of Geneva, Switzerland	YSM3811
Software and algorithms		
Fiji (ImageJ)	Schindelin et al.[52]	RRID:SCR_002285
Trainable Weka Segmentation	Arganda-Carreras et al.[53]	https://imagej.net/plugins/tws/
Cellpose	Stringer et al.[54]	RRID:SCR_021716
MATLAB	MathWorks	RRID:SCR_002285
Python	Python Software Foundation	RRID:SCR_008394

EXPERIMENTAL MODEL AND SUBJECT DETAILS

The model organism *Schizzosaccharomyces pombe* was used exclusively in this study, and all strains are listed in the key resources table. In this study, *S. pombe* cells were grown in yeast extract (YE5) medium or Edinburgh minimal medium with appropriate supplements at a temperature of 30°C.[55]

METHOD DETAILS

Construction of strains

The fission yeast strains used in this study are listed in Table S3. Strain VA078 was constructed by crossing PT2244 (h+ mmb1Δ:Kanr cox4-GFP:leu2 mCherry-atb2:Hygr ade6-m210 leu1-32 ura4-d18) with L972 (h- WT). Strain VA130 was constructed by crossing JFY3062 (h+ tom20-mCherry:NatR) with YSM3811 (h- ura4+::pact1: sfGFP-3RitCb: terminatortdh1 ade6-M210 leu+). VA131 was constructed by crossing crossed VA078 (h+ mmb1Δ:Kanr) with VA130 (h- ura4+::pact1:sfGFP-3RitCb:terminatortdh1 Tom20-mCherry:NatR). Strain VA132 was constructed by crossing PT592 (h- ase1::kanMX6 leu1-32 ura4-D18) with JFY3062 (h+ tom20-mCherry:NatR). Strain VA134 was constructed by crossing strain JFY2975 (h+ tom20-GFP:KanR) with L972 (h- WT). Strain VA135 was constructed by crossing VA132 (h-ase1::kanMX6 leu1-32 ura4-D18 Tom20-mCherry: NatR) with VA128 (h+ ura4+::pact1: sfGFP-3RitCb: terminatortdh1 leu-). Strain VA136 was constructed by crossing Dnm1Δ (h+ dnm1::kanr leu1-32ade-(ura+)) with VA130 (h- ura4+::pact1: sfGFP-3RitCb: terminatortdh1 Tom20-mCherry:NatR). Strain VA144 was constructed by crossing FY20823 (leu1 ura4 his7 Δklp5::ura4+ Δklp6::ura4+) with JFY3062 (h+ tom20-mCherry:NatR).

Preparing the YMM mold

The YMM design used in this study is identical to what was described in Nakaoka and Wakamoto.[24] We used an epoxy resin replica mold of the YMM which is a robust and cost-effective alternative to the traditional silicon wafer-based master mold.[25] To make the epoxy resin replica mold, first a PDMS (ProSci Tech; Cat. no.: CRI10837568) template was made from the silicon wafer-based master mold. A thin PDMS layer (10:1 monomer-to-cross-linker ratio) was cured in a Petri dish. The PDMS template was then plasma-cleaned, placed feature-side up on the cured PDMS layer, and covered with epoxy resin. After being degassed under a vacuum to remove air bubbles, the resin was allowed to fully cure. Finally, the Petri dish was removed using a Dremel tool and the PDMS template was carefully separated from the hardened epoxy. The resulting epoxy mold retained the microchannel pattern and served as a stable and reusable master mold for producing multiple YMM devices.

Preparing the YMM

A 10:1 PDMS mixture was degassed to remove bubbles that formed due to mixing, poured into the epoxy resin mold, and cured overnight at 65° C; the cured PDMS was peeled off, trimmed, and punched to form inlets/exit holes to allow the insertion of microfluidic tubing (Darwin microfluidics; Cat. no.:LVF-KTU-13). To remove dust particles from the surface of the coverslips, 24x60 mm coverslips (no. 1.5, ProSci Tech, Cat, no.: G425-4860) were soaked overnight in 1% SDS plus 0.1 M NaOH solution, rinsed with MilliQ water, sonicated in isopropanol for a couple of minutes and dried using nitrogen air to prevent liquid stains on the glass surface. Then both coverslips and PDMS devices were plasma-cleaned (feature side up), brought into contact, and placed in a 65° C oven for at least an hour to bond. Leak testing was performed in a custom 3D printed antileak chamber to ensure a stable, spill-free environment for extended time-lapse imaging.

Preparing *S. pombe* for imaging in the YMM

To populate the YMM with cells, the device was first wet with 0.01% Triton and thoroughly rinsed with YE5 medium. A highly concentrated cell suspension (nearly a cell pellet) was then loaded via a short piece of YMM tubing and a 5ml syringe fitted with a blunt needle. The cell filled device was centrifuged at 4000-4500 rpm (with rotation by 90° if necessary) until the microchannels were packed (~5 - 10 minutes). Excess cells were removed from the inlet and outlet holes using the short piece of YMM tubing and a syringe fitted with a blunt needle, allowing the outflow to rinse away stray cells without blocking the outlet. A peristaltic pump (Adelab Scientific, Cat. no.: NE-9000) was then attached to supply fresh YE5 medium and this was input into the YMM using fresh tubes in the inlet and outlet holes. As cells grew in lines within the YMM, any cells that were pushed out of the growth channels were washed away via the feeding channel.

Live-cell imaging using the YMM

To image *S. pombe* cells in the YMM, they were first acclimated by running the setup overnight on a Nikon confocal microscope (A1 or AX-R) using the built-in PFS feature to maintain focus. Faster flow rates (≥2 ml/h) helped align cells with the original cell (mother) trapped at the closed end of the channel while the progeny (daughters) escaped as the mother and daughters divided. Proper connections between the peristaltic pump and YMM tubing (via a needle and male luer) prevented leaks. Sufficient medium was provided to ensure continuous flow and cell viability. For strains lacking RitC:GFP, to delineate cell boundaries (PHP14 and VA144, see Table S3), YE5 media supplemented with 2μg/mL calcofluor white stain (Sigma-Aldrich cat. no.:18909) was continuously flowed into the YMM. The peristaltic tubing was replaced after each experiment and the flow rates of the pump recalibrated regularly. Confocal microscopy (Nikon A1 or AX-R, 60× water-immersion objective with 1.20 NA) was used to acquire z-stacks (1 μm intervals)

and time-lapse images (15 min intervals over 30–60 h) in transmitted light, 488 and 561 nm channels, captured both mitochondria (Tom20:mCherry) and cell boundaries (RitC:GFP).

MitoTracker and TMRE staining

For estimating mitochondrial volume in WT and *rho0* cells in Figures S5D and S5E, KI001 and PHP14 cells were grown overnight in a shaking incubator at 30°C, washed once with distilled water, and stained with 200nM and 400nM respectively of MitoTracker Orange CMTMRos (Thermo Fisher Scientific, cat. no. M7510) for 20 min. Following this, cells were washed with EMM and then allowed to adhere on lectin-coated (Sigma-Aldrich, cat. no. L2380) 35-mm confocal dishes (Mattek Corporation) for 20 min. TMRE staining was performed in a similar fashion, but VA134 and PHP14 cells were stained with 250nM TMRE (Thermo Scientific, cat. no. T669) before imaging. Mitochondrial volume was estimated as detailed below, and the total TMRE intensity per cell was estimated for Figure 5C, and mean intensity per pixel was estimated for Figure S5E from summed intensity projection of z-slices.

Measurement of surface area and volume of *S. pombe* cells

The surface area of the cell was calculated as follows:

$$\text{Surface Area} = 2\pi r L_{\text{total}}$$

where r is the radius of the cell, calculated as half of the width of the cell, L_{total} is the total measured cell length, including its hemispherical ends and π is the mathematical constant.

The volume of the cell was calculated as follows:

$$\text{Volume} = \pi r^2 L_{\text{total}} - \frac{2}{3}\pi r^3$$

QUANTIFICATION AND STATISTICAL ANALYSIS

Image Analysis

We developed an automated image analysis framework for segmenting and tracking *S. pombe* growing in the YMM using Fiji/ImageJ,[52] MATLAB (MathWorks Corp.), and Python. First, the fluorescent images of the YMM were cropped into individual channels and each channel was oriented with the closed end, containing the mother cell, at the bottom. Images with the closed end at the top were rotated 180° to maintain consistency. The images with fluorescent cell membranes were denoised with Nikon's AI-driven algorithm to remove Poisson shot noise and enhance the signal-to-noise ratio. The denoised images were then segmented using Cellpose, which is a deep learning tool trained on various cell morphologies.[54] Cells were segmented using either 'cyto2', 'cyto3', or a custom Cellpose model. In instances where the default cyto models produced segmentation errors on Calcofluor-stained images, a custom model was trained on the data to ensure segmentation accuracy. During segmentation, the diameter parameter was set to 'None', allowing the algorithm to automatically estimate the optimal cell size based on image characteristics. After segmentation, the 'regionprops' function in MATLAB extracted quantitative cell features (e.g. centroid, bounding box, length, width, and area).

We define cell birth as the moment the membrane (RitC:sfGFP) signal first appears at the medial plane of the cell, marking the onset of septum formation. This point also coincides with cell segmentation by Cellpose. In *S. pombe*, the septum, composed of specific polysaccharides, acts as a new cell wall that divides the two daughter cells.[52,56,57] During cytokinesis, septum formation physically separates the cytoplasm, enabling each daughter cell to grow independently.[58,59] Following septation, each daughter cell briefly passes through the G1 phase before entering the S phase to initiate its own DNA replication cycle.[60]

The cells were arranged by the y-coordinate of their centroids to identify and track the bottom-positioned mother cells. In the tracking algorithm, a decrease exceeding 30% in the area of a mother cell between consecutive frames was interpreted as a division event, which led the algorithm to visually mark the mother and daughter cells with bounding boxes. Each cell received a unique identifier (ID) recording its generation and lineage (e.g. mother cell '001' producing daughters '011' and '012', see Video S1). Mother cells were tracked continuously throughout the movie, while daughter cells were tracked until they underwent division. Finally, the areas/lengths of the mother and daughter cells were plotted, along with their mitochondrial intensities or volumes over time.

The mitochondrial channel was binarized using 3D Trainable Weka Segmentation in a two-class system, with mitochondria defined as one class and the background as the other.[53] For each FOV, a single representative 3D image was manually classified to construct a classifier model, which was then applied to all images in that time-lapse. Owing to differences in mean intensities between FOVs, a distinct classifier model was developed for each field. The mitochondrial area for each z-slice was determined using MATLAB's built-in function 'bwarea', which estimates the area of the objects in the binary image and then scaled by the corresponding pixel value. The mitochondrial volume was calculated by summing these area values across all z-slices and multiplying the sum by the inter-slice distance. For quantifying mitochondrial area and intensity, sum intensity projection images were used. The mitochondrial area was again extracted using 'bwarea' and scaled by the pixel value, while integrated density (which is the sum of all pixel intensities within

the region), was measured to determine mitochondrial intensity. To further ensure uniformity, all mitochondrial volume and intensity values were normalized using min-max normalization for each FOV, such that

$$M_{norm} = \frac{M - M_{min}}{M_{max} - M_{min}}$$

Where M_{max}: highest mitochondrial volume measured in that FOV and M_{min}: lowest mitochondrial volume measured in that FOV. This ensured that all FOVs had mitochondrial volumes between 0 and 1. Wherever mitochondrial volume measured from cells grown in the YMM has been plotted in this manuscript, it refers to this min-max normalized mitochondrial volume.

Statistical analysis

All plots were generated in MATLAB. For population-wide patterns and comparisons between WT and mutant strains (Figures 1C, 1D, 2C, 3A–3C, 3E, 3F, 5C, S2C–S2E, S3, S4B–S4D, and S4J), raw values were rescaled by normalizing to their respective means (e.g., in Figure 2C, the birth lengths were divided by the mean birth length, and the mitochondrial volumes at birth were divided by the mean mitochondrial volume at birth). In Figures 5 and S5, cells included in the plots have cell cycle durations within 1 SD of the mean duration of the WT or *rho0* cell cycle; the instantaneous growth rates are plotted from the time that the cells separate. For comparison between WT and *rho0* cells, time was normalized to the maximum cell duration plotted since *rho0* cells have a much longer duration than WT cells.

Heat scatter plots were created using a custom MATLAB function[61] to depict local data density with a colour map (warmer colours indicate higher density). Data were grouped into bins, and outliers were removed using MATLAB's 'rmoutlier' function. Trend lines were fit using MATLAB's 'cftool' with a Linear Model ('Poly1') and each point weighted by the inverse of its SEM. Shaded error plots, showing the mean with SEM or SD shading, were generated using the custom 'shadedErrorBar' function,[62] with similar fitting procedures. For all the shaded error bar plots involving the mutants, 5 bins were used. Data were checked for normality using the 'chi2-gof' function in MATLAB. Then, to test the statistical significance of the difference between distributions we used ordinary one-way ANOVA or Student's T-test for parametric data and Kruskal-Wallis test, or Mann-Whitney test for non-parametric data. The figures were organized and prepared in Illustrator.

Current Biology, Volume *35*

Supplemental Information

Mitochondrial function regulates cell growth kinetics to maintain mitochondrial homeostasis

Leeba A. Chacko, Hidenori Nakaoka, Richard G. Morris, Wallace F. Marshall, and Vaishnavi Ananthanarayanan

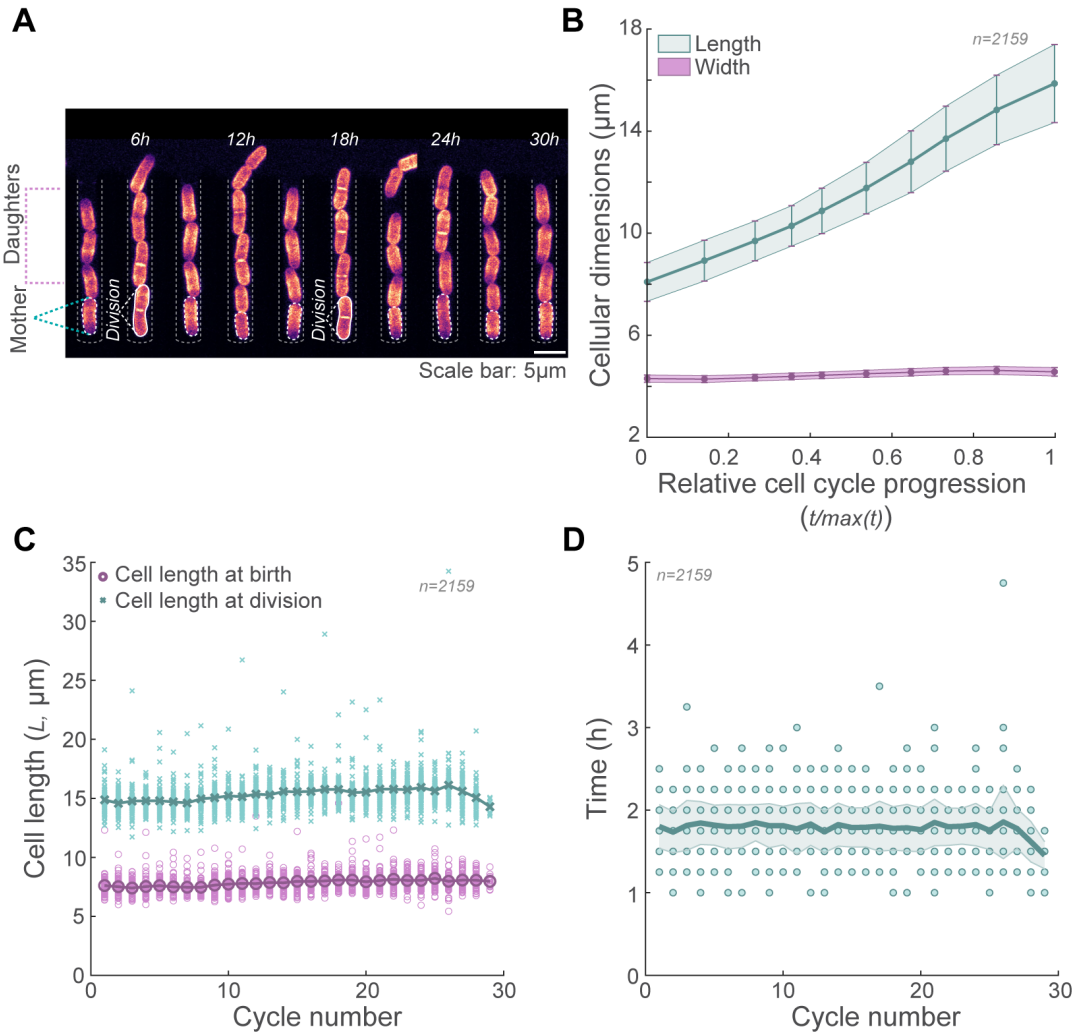

Figure S1. Cell growth is optimal in the YMM, Related to Figure 1, Table S1 and Video S1. **(A)** Montage of cells expressing a fluorescent membrane marker (RitC:GFP) growing in a single channel of the YMM, showing representative mother and daughter cells, as well as division events. **(B)** Plot depicting changes in cell length and width (mean ± SD) and within the YMM during the cell cycle (represented as relative cell cycle progression, *t/max(t)*), **(C)** Plot of the raw (scatter) and mean (solid line) cell lengths (L) of WT cells growing in the YMM at birth (magenta) and at division (teal), **(D)** Plot of the individual cell cycle durations (circles) and mean ± SD (solid line and shaded region respectively) of WT cells growing in the YMM. Strain VA130 was used in this figure, see Table S3.

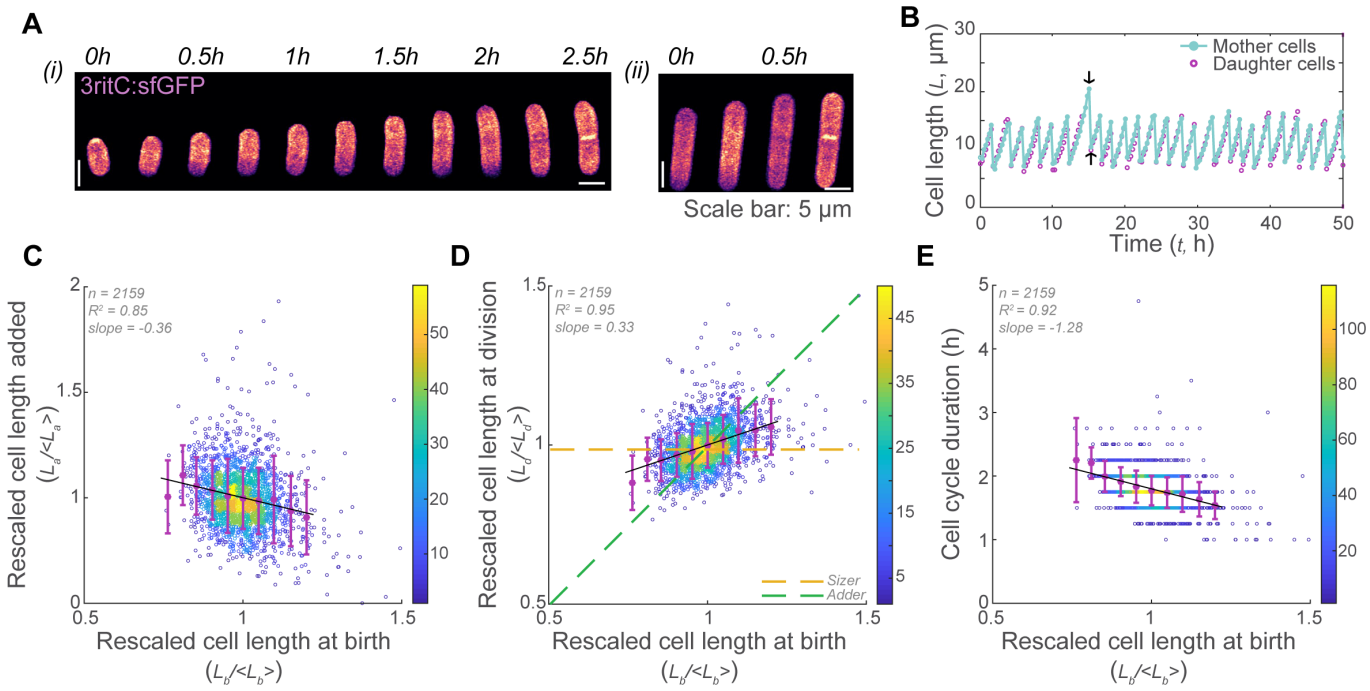

Figure S2. ***S. pombe*** **cells show sizer-like behaviour, Related to Figure 1 and Table S1**. **(A)** Example montages of an entire cycle of cells expressing a fluorescent membrane marker with different sizes at birth: (i)small cell and (ii) large cell. **(B)** Example plot of cell length (L) over time (t) in WT cells growing in the YMM showing cell length fluctuations. The arrow heads point to a cell with increased length at division (top arrowhead) and birth (bottom arrowhead), **(C)** Rescaled cell length added during the cycle $(L_a/ < L_a >)$ plotted against the rescaled cell length at birth $(L_b/ < L_b >)$ shows an inverse relationship, **(D)** Rescaled cell length at division $(L_d/ < L_d >)$ plotted against the rescaled cell length at birth shows a sizer-like behaviour. The yellow dashed line represents the expected data for a perfect sizer and the green dashed that for an adder, **(E)** The cell cycle duration plotted against the rescaled cell length at birth shows that cells that are smaller at birth spend more time in the cell cycle. The data in **C**-**E** were rescaled to the mean of the parameters plotted as indicated in the axis labels. In **C**-**E**, error bars represent the SD and the heat map represents the density of the data. Strain VA130 was used for all the figures in this panel (see Table S3).

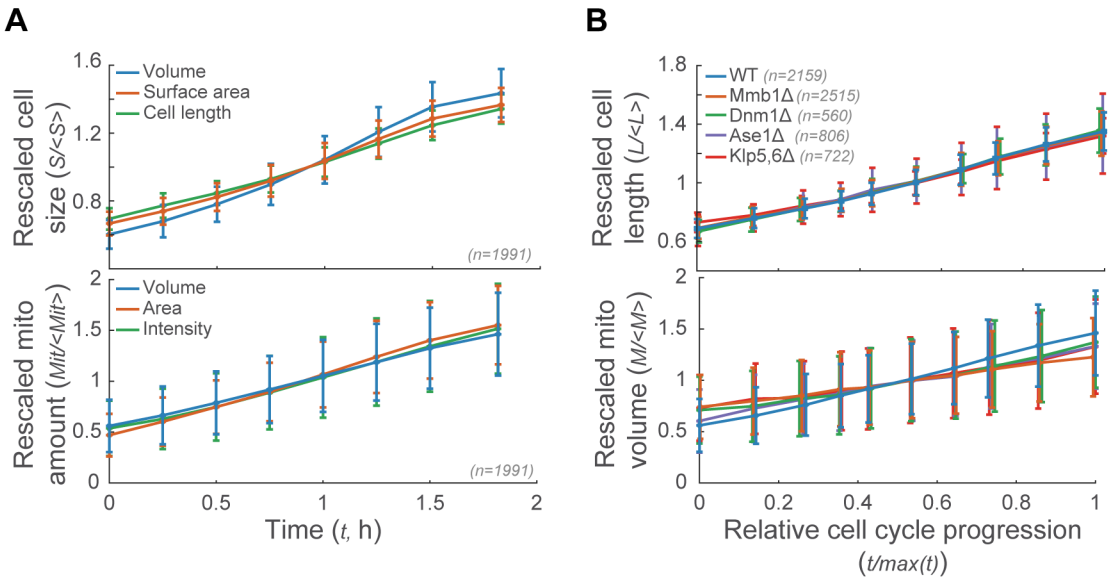

Figure S3. The mitochondrial amount grows with cell size, Related to Figure 2 and Video S3. **(A)** Plots of rescaled cell size (cell volume, surface area and length, $S/ < S >$) over time (t, top) and the rescaled mitochondrial amount (mitochondrial volume, area and intensity, $Mit/ < Mit >$) over time (t, bottom). The error bars represent the mean $\pm$ SD. The volume and surface area of the cell were calculated as detailed in the Methods section. Strain VA130 was used for this panel (see Table S1). **(B)** Plots of rescaled cell length ($L/ < L >$,top) and the rescaled mitochondrial volume ($M/ < M >$, bottom) over the relative cell cycle progression ($t/ < max(t) >$). The solid lines represent the mean and the error bars SD. The data in this figure were rescaled to the mean of the parameters plotted as indicated in the axis labels. Strains VA130, VA131, VA136, VA135, and VA144 were used for for this panel (see Table S3).

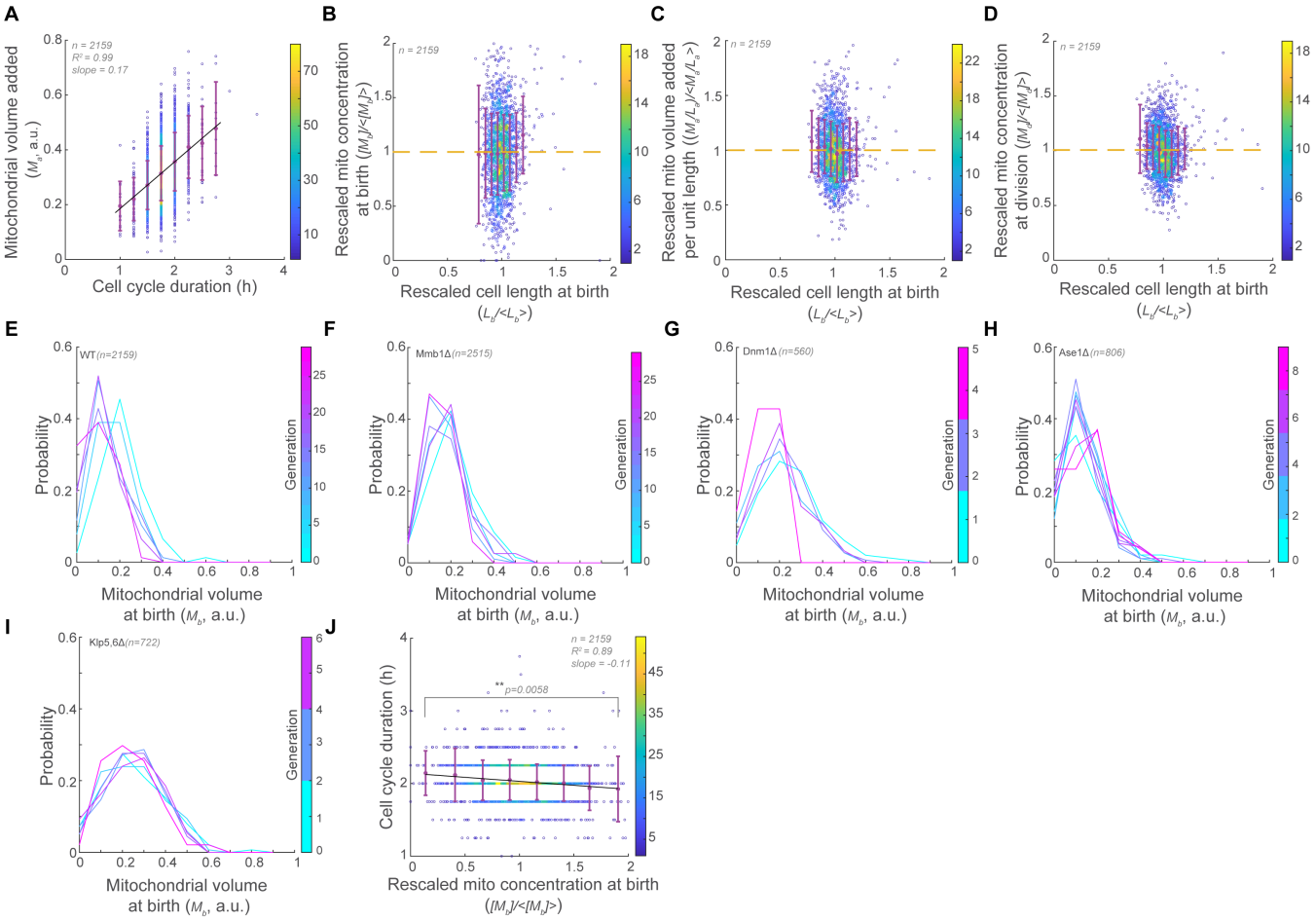

Figure S4. WT and mutant cells correct for errors in mitochondrial partitioning within a single generation, Related to Figure 3 (A) The mitochondrial volume added per cycle (M_a) and the duration of cell cycle in WT cells show a linear relationship, i.e., longer the cell cycle, more the mitochondrial volume added before division. **(B)** Rescaled mitochondrial concentration at birth ($[M_b]/<[M_b>]$) plotted against the rescaled cell length at birth ($L_b/<L_b>$) in WT. **(C)** Rescaled mitochondrial volume added per unit length ($[M_a]/<[M_a]>$) added during the cell cycle plotted against the rescaled cell length at birth in WT cells. **(D)** Rescaled mitochondrial concentration at division ($[M_d]/<[M_d]>$) plotted against the rescaled cell length at birth in WT. Histogram of mitochondrial volume at birth (M_b) for multiple generations of **(E)** WT, **(F)** Mmb1Δ, **(G)** Dnm1Δ, **(H)** Ase1Δ, and **(I)** Klp5,6Δ cells tracked in the YMM. The data in **E** and **F** were plotted for every fifth generation. **(J)** Plot of cell cycle duration against the rescaled mitochondrial concentration at birth. In **A**-**D** and **J**, error bars represent SD. The black solid lines represent a linear fit to the data; the heat map represents the density of the data. The cell cycle durations were significantly lower in cells with higher mitochondrial concentrations at birth (last bin) compared to cells with lower mitochondrial concentrations (first bin, $^{**}p = 0.0058$, Mann-Whitney U test for non-parametric data). The data in **A**-**D** and **J** were rescaled to the mean of the parameters plotted as indicated in the axis labels. Strains VA130, VA131, VA136, VA135, and VA144 were used for for this panel (see Table S3).

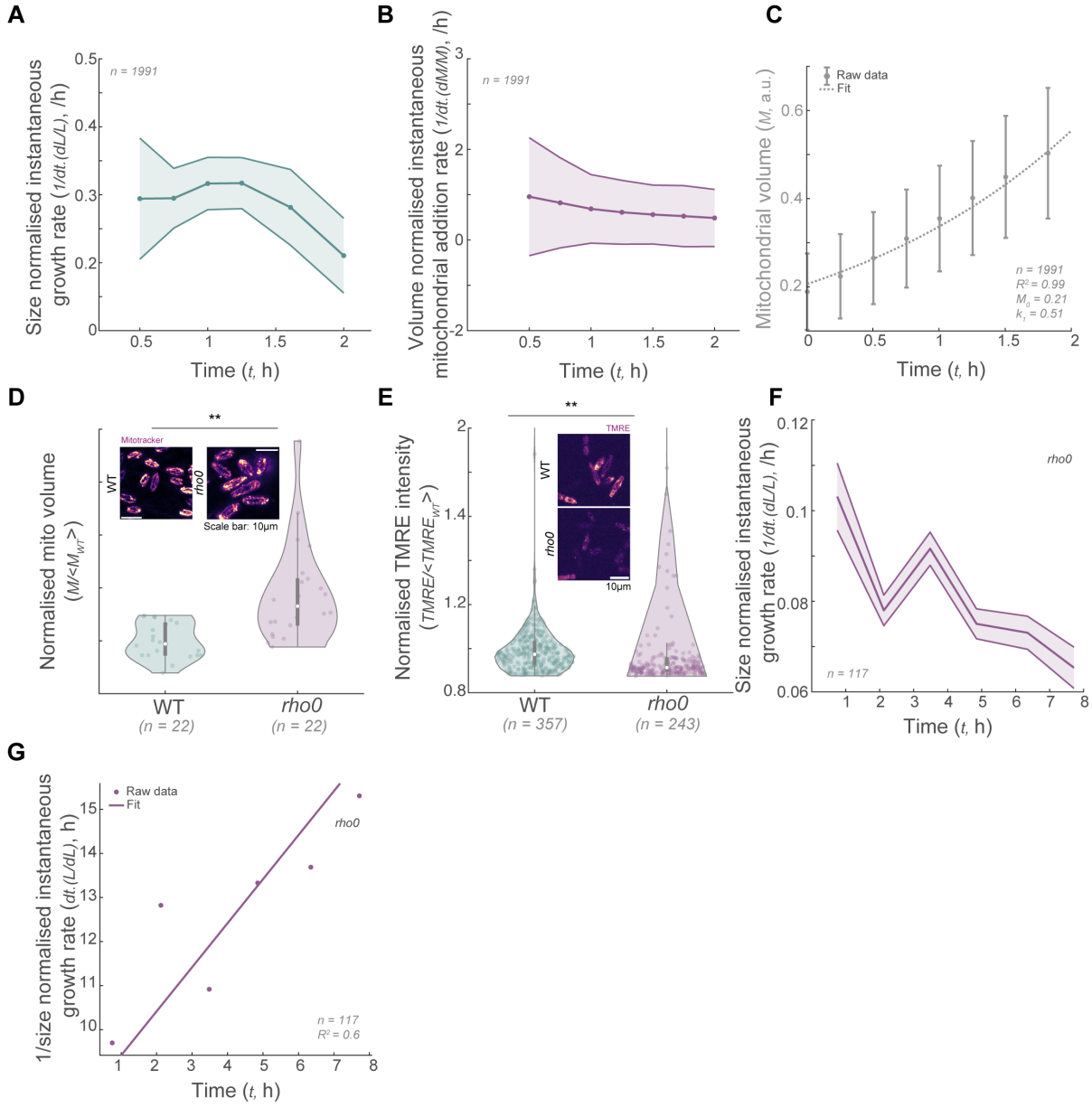

Figure S5. Mitochondrial activity leads to exponential growth of cells, Related to Figure 5 (A) Plot of size-normalised instantaneous growth rate $(1/dt.(dL/L))$ of WT cells over time (t), **(B)** Plot of volume-normalised instantaneous mitochondrial addition rate $(1/dt.(dM/M))$ over time in WT cells. In A and B, the solid line represents the mean and the shaded region represents the SD, **(C)** Plot of mitochondrial volume over time fit to an exponential curve. Error bars represent SD, **(D)** Mitotracker-stained images of WT and *rho0* mitochondria (inset), and plot of normalised mitochondrial volume $(M/ < M_{WT} >)$ in WT and *rho0* cells. *Rho0* cells had higher mitochondrial volumes; this fit with the scaling of mitochondrial volume with cell size, since *rho0* are significantly larger than WT cells (see Table S1). Asterisks represent significant difference ($^{**}p < 10^{-4}$), student's T-test for parametric data. **(E)** TMRE-stained images of WT and *rho0* mitochondria (inset), and plot of normalised total TMRE intensity (*TMRE/<TMRE*$_{WT}$*>*) in WT and *rho0* cells. *Rho0* cells showed significantly lower TMRE intensity and thus mitochondrial activity compared to WT cells. Asterisks represent significant difference ($^{**}p < 10^{-3}$), student's T-test for parametric data. The data in **D** and **E** were normalised to the mean of the WT parameters as indicated in the axis labels. **(F)** Plot of size-normalised instantaneous growth rate $(1/dt.(dL/L))$ of *rho0* cells over time (t). For cells growing linearly with a rate k, the length is given by: $L(t) = l_0 + kt$; $with\ dL/dt = k$. The size-normalised growth rate $\lambda(t) = k/L(t) = k/(l_0 + kt)$. Rewriting: $\lambda(t) = 1/(A + t)$, where $A = l_0/k$. Transforming this hyperbolic equation to a linear form gave $1/\lambda(t) = t + A$. This enabled us to perform linear regression of the reciprocal of the size-normalised growth rate $(1/\lambda(t))$ v time (t) for *rho0* cells. **(G)** Plot of the reciprocal of size-normalised instantaneous growth rate (solid circles) of *rho0* cells over over time, and a linear fit to the data (solid line). For linearly growing cells, we expect to observe a linear relationship between 1/size-normalised growth rate and time, and indeed we observed a scaling of $1/\lambda(t)$ with time in *rho0* cells indicating that *rho0* cells indeed switched to linear growth in the absence of mtDNA. Strains VA130, VA131, KI001, VA134 and PHP14 were used for for this panel (see Table S3)

Strain	**Cell length at birth** (mean $\pm$ SD) μm	**Cell length at division** (mean $\pm$ SD) μm	**Cell cycle duration** (mean $\pm$ SD) h	**Number of cells** (n)
WT	8.1 ± 0.8	15.8 ± 1.4	1.8 ± 0.3	2159
Mmb1Δ	7.9 ± 0.8	15.3 ± 1.4	2.0 ± 1.9	2515
Dnm1Δ	7.4 ± 0.9	14.9 ± 1.6	2.0 ± 0.4	560
Ase1Δ	7.6 ± 1.1	14.8 ± 2.4	1.9 ± 0.4	806
Klp5,6Δ	7.8 ± 0.7	14.1 ± 1.2	1.8 ± 0.3	722
rho0	9.8 ± 1.4	18.5 ± 2.9	9.3 ± 4.9	158

Table S1. Measured parameters for WT and mutant cells, Related to Figure 1 and Figure S1.

Strain	$\mathbf{R^2}$	Slope	n
Figure 1C			
WT	0.98	-1.47	2159
Mmb1Δ	0.99	-1.87	2515
Dnm1Δ	0.98	-1.83	560
Ase1Δ	0.93	-2.77	806
Klp5,6Δ	0.99	-1.39	722
Figure 1D			
WT	0.99	0.31	2159
Mmb1Δ	6.4×10^{-5}	0	2515
Dnm1Δ	0.75	0.07	560
Ase1Δ	0.14	-0.05	806
Klp5,6Δ	0.98	0.31	722
Figure 2C			
WT	0.99	1.13	2159
Mmb1Δ	0.99	0.99	2515
Dnm1Δ	0.92	0.85	560
Ase1Δ	0.99	1.52	806
Klp5,6Δ	0.97	0.75	722
Figure 3E			
WT	0.99	-0.77	2159
Mmb1Δ	0.99	-0.81	2515
Dnm1Δ	0.85	-0.04	560
Ase1Δ	0.94	-0.7	806
Klp5,6Δ	0.99	-1.21	722
Figure 3F			
WT	0.93	-0.07	2159
Mmb1Δ	0.99	0.22	2515
Dnm1Δ	0.89	0.38	560
Ase1Δ	0.87	0.21	806
Klp5,6Δ	0.72	-0.17	722

Table S2. Goodness of fits ($\mathbf{R^2}$) and slopes for mutant data, Related to Figures 1, 2 and 3.

Name	Genotype	Source
Dnm1Δ	h- dnm1::kanr leu1-32ade-	Yannick Gachet, Toulouse
FY20823	h- leu1 ura4 his7 Δklp5::ura4+ Δklp6::ura4+	YGRC, Japan
JFY2975	h+ tom20-GFP:KanR	Jonathan Friedman, UT Southwestern, Dallas, Texas, USA
JFY3062	h- tom20-mCherry:NatR	Jonathan Friedman, UT Southwestern, Dallas, Texas, USA
KI001	h+ sid4-GFP::kan r kan r -nmtP3-GFP-atb2+ nmt1-pCOX4-RFP::leu1+ ura4-D18 ade6-M210	Iva Tolić
L972	h- WT	Iva Tolić
PHP14	h- rho0 ade6M-216 leu1-32 ptp1-1	Thomas Fox, Cornell University, USA
PT2244	h+ mmb1Δ:Kanr cox4-GFP:leu2 mCherry- atb2:Hygr ade6-m210 leu1-32 ura4-d18	Phong Tran, University of Pennsylvania, USA
PT592	h- ase1::kanMX6 leu1-32 ura4-D18	Phong Tran, University of Pennsylvania, USA
VA078	h+ mmb1Δ:Kanr	This paper
VA128	h+ ura4+::pact1:sfGFP-3RitCb:terminatortdh1 leu-	This paper
VA130	h- ura4+::pact1:sfGFP-3RitCb:terminatortdh1 Tom20-mCherry:NatR	This paper
VA131	h+ mmb1Δ:Kanr ura4+::pact1:sfGFP-3RitCb:terminatortdh1 Tom20-mCherry:NatR	This paper
VA132	h- ase1::kanMX6 leu1-32 ura4-D18 Tom20-mCherry:NatR	This paper
VA134	h- Tom20-GFP:KanR	This paper
VA135	h- ase1::kanMX6 Tom20-mCherry:NatR ura4+::pact1:sfGFP-3RitCb:terminatortdh1	This paper
VA136	h+ dnm1::kanr ura4+::pact1:sfGFP-3RitCb:terminatortdh1 Tom20-mCherry:NatR	This paper
VA144	h- Δklp5::ura4+ Δklp6::ura4+ Tom20-mCherry:NatR	This paper
YSM3811	h- ura4+::pact1:sfGFP-3RitCb:terminatortdh1 ade6-M210 leu+	Sophie Martin, University of Geneva, Switzerland

Table S3. List of strains used in this paper, Related to Figures 1-5, Figures S1-S5.